This is to certify that the
thesis entitled

DEVELOPMENT AND CHARACTERIZATION OF AN OPTICAL FEEDBACK CONTROLLED MICROPHONE FOR AEROACOUSTICS RESEARCH

presented by

Eliott Radcliffe

has been accepted towards fulfillment
of the requirements for the

Masters degree in Mechanical Engineering

Major Professor's Signature

8/26/2010

Date

MSU is an Affirmative Action/Equal Opportunity Employer

DEVELOPMENT AND CHARACTERIZATION OF AN OPTICAL FEEDBACK CONTROLLED MICROPHONE FOR AEROACOUSTICS RESEARCH

By

Eliott Radcliffe

A THESIS

Submitted to
Michigan State University
in partial fulfillment of the requirements
for the degree of

MASTER OF SCIENCE

Mechanical Engineering

2010

ABSTRACT

DEVELOPMENT AND CHARACTERIZATION OF AN OPTICAL FEEDBACK CONTROLLED MICROPHONE FOR AEROACOUSTICS RESEARCH

By

Eliott Radcliffe

This study constitutes a proof of concept of a new feedback-controlled optical microphone for potential use in phased "beamforming" arrays utilized in aeroacoustics research. In the new microphone design, an optical sensor is employed as a means for measuring the center displacement of a stretched thin membrane caused by incident acoustic pressure. The membrane is constructed from PVDF (polyvinylidene-fluoride) which exhibits piezoelectric properties allowing actuation of the membrane in a feedback system, where force feedback is used to nullify the optically detected deflection. The feedback provision was used to actively modify sensor parameters, most notably membrane stiffness, resonant frequency, and damping. A theoretical study is presented to examine the viability of two improvements that may be used in future microphone designs. Implementation of one or both of these improvements is expected to significantly increase controllability of the feedback-controlled optical microphone documented here.

DEDICATION

This thesis is dedicated to family, friends, and anyone else who has helped me along my way, and shaped the person I am today. I'd like to extend special gratitude to Dr. Naguib who has been absolutely everything that I could have ever hoped for in a faculty advisor. His combination of genuine understanding and shared wisdom has put me in the best possible position to be successful. Also, to Tony Humphreys for believing enough in the research to sponsor a GSRP fellowship for two years, and for bringing me to the grand facility that is NASA Langley Research Center.

To my parents, you have been there for me every step of the way, and I know will continue to be. For this I am eternally grateful. To Nate and Terri and my beautiful niece Kaelyn. To Isa and Justin, my nephew Owen, and one more on the way. Finally, to my grandparents and extended family, with special mention to Charles Radcliffe, the patriarch of a long line of Radcliffe engineers.

Lastly, I'd like to thank my closest friends from my college years and beyond. In no particular order, Jesse, Dan, Adam, Ashley, Alan, Dave, Nick, Stacy, Noah, Jenny, Liz, Molly, Godwin, Zach, Jill, Megan, Jess, Will, and Derek. As many of us are beginning a new chapter in our lives and embarking to distant locales across the country and world, I hope we all remember where we came from and return home to Michigan whenever we can find the time.

And if I don't see you for a long while, I'll come and find you left of the dial.
-Paul Westerberg

ACKNOWLEDGMENT

This work is generously supported by the NASA GSRP fellowship, grant no NNX08AO07H. Additionally, gratitude is extended towards Dr. Allan Zuckerwar at NASA Langley Research Center for his shared expertise in fibre-optic sensing and microphone design.

TABLE OF CONTENTS

List of Tables viii

List of Figures ix

Key to Symbols and Abbreviations xiii

1 Introduction **1**
1.1 Motivation 1
1.2 Previous Feedback-Controlled Microphones 5
1.3 Description of Current Research 6

2 A Novel Feedback-Controlled Optical Microphone using a Commercial Fiber-Optic Sensor **9**
2.1 Microphone Construction and Feedback System Components 9
2.1.1 PVDF Film Microphone Capsule 9
2.1.2 Fiber-Optic Lever Displacement Sensor 11
2.1.3 Feedback System Components 12
2.2 Analytical Modeling 13
2.3 Experimental Procedure 19
2.4 Results and Discussion 22

3 A Feedback-Controlled Optical Microphone Incorporating a Michelson Interferometer **31**
3.1 Construction 32
3.1.1 Microphone Membrane 32
3.1.2 Michelson Interferometer 34
3.1.3 Serial Interfaced Controller 38
3.2 Experimental Procedure 41
3.3 Results and Discussion 43
3.3.1 Electrical Actuation 43
3.3.2 Acoustic Calibration 44
3.3.3 Comparison of Michelson Interferometer to Fiber-Optic Lever Sensor 48

4 Theoretical and Experimental Evaluation of Proposed Design Improvements **50**
4.1 Displacement Averaging Optical Sensor 51
4.2 Perforated Back-Plate 58

5 Summary and Conclusions **69**

6 Appendix **73**
6.1 Appendix A - Electrical Circuits 73
6.1.1 Phase-Lead Compensator Circuits 73
Compensator Circuit #1 74
Compensator Circuit #2 74
Compensator Circuit #3 75
6.1.2 Michelson Interferometer Control Circuit 80
6.1.3 Other Circuits 81
Signal Amplifier and Variable Low Pass Filter 81
Third Order Inverse Chebyshev Filter 82
Power Amplifier 84
6.2 Appendix B - Software Applications 84
6.2.1 FeedbackGUI 84
Calibration stage 85
System Identification Stage 86
Closed-Loop Specification Stage 87
Controller Programming Stage 87
6.2.2 MATLAB Software 88
PhaseLeadGUI 88
DigitalPot.m 88
Perforated Backplate GUI 89
PLC_Solver.m 89
EstimateMembrane.m 90

Bibliography **91**

LIST OF TABLES

2.1 Design equations for compensator circuit. Resisters are represented by $R_{p1}, R_{p2}, R_{d2}, R_{DC}$, and, $R_{f,sum}$, while potentiometers R_p, R_c, R_d control proportional gain, derivative time constant, and derivative gain. A fixed capacitance is represented by C. 18

2.2 Microphone parameters for open-loop operation 24

3.1 Comparison of sensor parameters between fiber-optic lever and Michelson interferometer. 49

4.1 Average relative displacement of membrane vibrational modes over the entire surface of the membrane. 53

4.2 Known or measured parameters of the acrylic inserts used for verification of the mechanical damping model. 64

4.3 Calculated parameters of the acrylic inserts used for verification of the mechanical damping model. 65

6.1 Electrical components used in phase-lead controller circuit depicted in Figure 2.4 77

6.2 Electrical components used in serial interfaced phase-lead controller depicted in Figure 3.7 80

6.3 Electrical components used in Michelson interferometer control circuit depicted in Figure 3.6 82

LIST OF FIGURES

Images in this thesis are presented in color

1.1 Drawing of a typical commercial condenser microphone (p is the acoustic pressure which causes a proportional movement in the membrane). 3

1.2 Drawing of a typical commercial electret microphone. 3

2.1 Schematic drawing of prototype microphone capsule: exploded (left) and assembly (right) views. 10

2.2 Schematic drawing of fiber-optic lever probe. 12

2.3 Control block diagram for optical feedback controlled microphone system. Note that P, Z_c, Z_{cr} and V are the Laplace transforms of the acoustic pressure, actual and reference central membrane deflection, and output voltage respectively. 13

2.4 Schematic diagram of circuit used for implementation of the phase-lead compensator. 17

2.5 Schematic diagram of the plane wave tube calibration setup. 21

2.6 Electrical response of PVDF membrane for variation of internal static pressurization: (top) actuation sensitivity of PVDF membrane; (bottom) fundamental resonance frequency of PVDF membrane. 23

2.7 Frequency response of PVDF membrane identified using electrical actuation with 1.5kPa internal pressurization: (top) Actuation sensitivity of PVDF membrane; (bottom) Phase response of PVDF membrane . 25

2.8 Response of microphone in open-loop and closed-loop operation for the design specification of 0dB attenuation, β=95°, and $f_{0,CL}$=5.1kHz: (top) acoustic sensitivity; (bottom) phase 27

2.9 Response of microphone in open-loop and closed-loop operation for the design specification of 3dB attenuation, β=92.5°, and $f_{0,CL}$=4.8kHz: (top) Acoustic sensitivity; (bottom Phase 28

2.10 Linearity and noise floor for open- and closed-loop operation. 29

3.1 Depiction of 6.35mm diameter membrane prototype, top: top view, bottom: side view. 33

3.2 Front view depiction of 6.35mm diameter membrane prototype with acrylic channel (PWT) attached. 34

3.3 Depiction of the optical setup for the Michelson interferometer. 35

3.4 Photograph of the optical setup for the Michelson interferometer (Note the placement of a CCD camera and mirrors which aid in alignment of the laser beam with the center of the microphone membrane). 36

3.5 Inteferometer output relative to mirror displacement. 37

3.6 Schematic diagram of interferometer circuit, with feedback section. . . 38

3.7 Schematic diagram of phase-lead controller circuit. 39

3.8 Schematic diagram of serial potentiometer interface. 40

3.9 Frequency response of 6.35mm membrane with Michelson interferometer, measured using electrical actuation. 43

3.10 Frequency response of 6.35mm membrane with Michelson interferometer, measured using electrical actuation, magnified to show frequencies near the fundamental resonance. 45

3.11 Frequency response of 6.35mm membrane with Michelson interferometer, measured using acoustic calibration in a plane wave tube. 46

3.12 Linearity of 6.35mm membrane with Michelson interferometer, measured using acoustic calibration in plane wave tube at 3kHz and 12kHz. 48

4.1 Axi-symmetric mode shapes of a vibrating membrane. 52

4.2 Average relative displacement of membrane vibrational modes over the entire surface of the membrane. 53

4.3 Relative average displacement of membrane as a function of the sensor probe diameter. 54

4.4 Theoretical frequency response of the open-loop when measuring the membrane deflection at its center (solid line) compared to when using an optical sensor with a_s/a =0.37 56

4.5 Theoretical frequency response of the open-loop when measuring the membrane deflection at its center (solid line) compared to when using an optical sensor with a_s/a =0.69 57

4.6 Equivalent circuit of the perforated back-plate and back-chamber. . . 60

4.7 Schematic drawing of prototype microphone capsule with acrylic insert designed to simulate a perforated back-plate. 64

4.8 Experimental frequency response of microphone membrane with perforated inserts where the number of holes is varied. 65

4.9 Experimental frequency response of microphone membrane with improved perforated insert. 67

4.10 Depiction of GUI application used for perforated back-plate design, with "ideal" design of back-plate shown. 68

6.1 Schematic diagram of first phase-lead compensator circuit. 75

6.2 Photograph of front panel of first phase-lead compensator circuit. . . 76

6.3 Photograph of second phase-lead compensator on a breadboard. . . . 76

6.4 Photograph of third phase-lead compensator circuit. 77

6.5 Example digital waveform used in programming a MCP42XXX series digital potentiometer. The example case is for programming potentiometer 0 to position 50, where the full 16 bit input is 00010001 00110010. 79

6.6 Photograph of Michelson interferometer control circuit. 81

6.7 Schematic diagram of signal amplifier and variable low pass filter circuit. 83

6.8 Photograph of signal amplifier and variable low pass filter circuit. . . 83

6.9 Photograph of inverse Chebyshev filter circuit. 84

6.10 Photograph of 386 power amplifier circuit. 85

KEY TO SYMBOLS AND ABBREVIATIONS

a	Membrane radius
A	Membrane surface area
a_s	Optical sensor radius
a_0, a_1, b_1	Phase lead compensator parameters
C_0	Damping of fundamental resonant mode
C_{0b}	Damping term added by the perforated back-plate for the zeroth mode
C_m	Damping of m^{th} resonant mode
c_T	Isothermal speed of sound in air
f_0	Fundamental resonant frequency in Hz
$G_C(s), G_O(s), G_{PZ}(s)$	Transfer functions of compensator, optical sensor, and piezoelectric system
$H(s)$	Membrane transfer function
$\|H_{act}(\omega)\|$	Frequency response function of membrane deflection relative to applied voltage
$J_0(r)$	Bessel function of the zeroth order
K_0	Stiffness of fundamental resonant mode
k_m	Wave number of m^{th} membrane axi-symmetric mode
K_m	Stiffness of m^{th} resonant mode
K_d	Derivative gain
K_{0b}	Stiffness term added by back-chamber for the zeroth mode
K_p	Proportional gain
l_k	Length of hole in perforated back-plate

M	Membrane mass (surface density)
M_{0b}	Inertial mass term added by perforated back-plate for the zeroth mode
N	Number of modes retained in the membrane transfer function
p	Acoustic pressure
PWT	Plane wave tube
P_b	Back-chamber pressure vector
p_k	Acoustic pressure at k^{th} hole in back-plate
$P(s)$	Acoustic pressure Laplace transform
q	Number of holes in the perforated back-plate
r	Radial coordinate on membrane
r_k	Radius of hole in perforated back-plate
SPL	Sound pressure level
s_1	Complex pole of the closed-loop transfer function
S_M	Microphone sensitivity
S_{act}	Membrane electrical actuation sensitivity at low frequency
S_H, S_O, S_C, S_{PZ}	Sensitivity of membrane, optical sensor, compensator, and piezoelectric system
t	Time
T	Membrane tension (force per unit length)
U_b	Air volume velocity vector
u_k	Air volume velocity at k^{th} hole in back-plate
u_k	Air volume velocity at k_{th} hole

V	Voltage
$V(s)$	Voltage Laplace transform
z	Membrane deflection perpendicular to surface
z_{avg}	Membrane deflection averaged over the entire surface of the membrane
Z_b	Acoustic impedance matrix relating to perforated back-plate and back-chamber
z_c	Membrane deflection measured at its center
Z_C	Acoustic impedance of the back-chamber
z_{cr}	Membrane center deflection reference
$Z_c(s)$	Membrane center deflection Laplace transform
β	Polar angle of the complex pole of the closed-loop transfer function, measured from the positive real axis
γ	Specific heat ratio of air
ζ_0	Damping ratio of fundamental resonant mode
$\zeta_{0,CL}$	Damping ratio of fundamental resonant mode in closed-loop operation
θ	Angular coordinate on membrane
λ	Wavelength of light
μ	Viscosity of air
ρ_s	Membrane surface density (mass per unit area)

ρ_0	Density of air
τ_d	Time constant corresponding to derivative gain cutoff
ϕ_{vz}, ϕ_{vv}	Cross-spectrum between membrane deflection and voltage input and auto-spectrum of voltage input
ψ	Polar angle of $H(s_1)G_O(s_1)G_{PZ}(s_1)$
ω	Angular frequency (radians/s)
ω_0	Fundamental natural frequency (radians/s)
$\omega_{0,CL}$	Fundamental natural frequency in closed-loop operation (radians/s)
ω_H, ω_L	Half-power frequencies (radians/s)

Chapter 1

Introduction

1.1 Motivation

A great deal of current research is taking place in the field of aeroacoustics, with studies being performed to characterize noise sources such as aircraft wings, landing gear, and jet engines. Tests are performed in widely varying environments ranging from acoustically treated quiet flow facilities to aircraft fly-overs. One particular technology that has been developed for this purpose is the "beamforming" microphone array. These arrays contain large sensor counts, typically ranging from approximately 30 to over 100. The operating principle of these arrays derives from the propagation delay from a noise source to a given sensor in the array. Knowledge of the delay time for each microphone in the array can be exploited to resolve the location of an acoustic source. The classical beamforming method involves discrete time-shifting of each digitally acquired microphone signal for localization of acoustic sources, while more modern methods use deconvolution and frequency domain based signal processing [1],[2].

Regardless of the method of analysis, it is important to have accurate knowledge of the frequency response of each microphone in the system, particularly with regard to phase. Typically, microphones are calibrated before any experiments such that any mismatch in the response of individual units may be accounted for. Difficulties arise due to the time consuming nature and equipment required for acoustic calibration. Furthermore, a calibration performed in a laboratory setting may be rendered invalid when the sensor is used in field testing where it is exposed to effects such as heat and humidity.

Various microphone technologies are currently implemented in beamforming arrays. Perhaps most common is the use of an instrument grade condenser microphone. A drawing of this type of microphone is shown in Figure 1.1. The operating principle for the condenser microphone is that the capacitance between a stretched, pressure sensitive membrane and conductive back-plate varies as a result of membrane motion. A typical gap between the back-plate and membrane is approximately 25 μm. When a fixed charge is applied to the back-plate, these changes in capacitance result in a varying voltage at the back-plate. This charge is maintained by a large (typically 28V-200V) polarization voltage which is connected to the plate through a resistor [3]. Additional features include an annular slot around the back-plate, in addition to holes to increase damping of the membrane motion. Also, a capillary vent hole is included for equalization of static air pressure in the back-chamber with the atmosphere. Commercial condenser microphones are available that are individually calibrated by the manufacturer and guaranteed to have a high degree of phase uniformity ($\pm 10^\circ$ at 10kHz)[1]. However, the cost per channel for a high-quality capsule is very high (approximately $2000).

[1] Datasheet - Brüel & Kjaer Type 4958 20kHz Precision Array Microphone

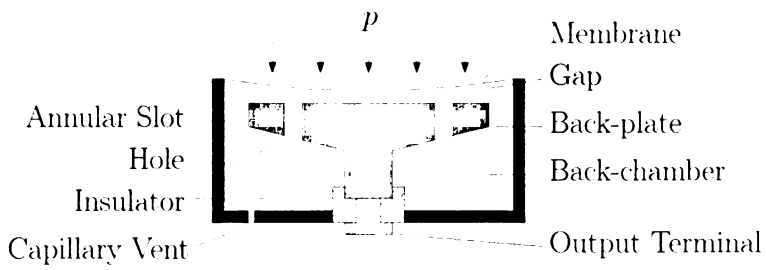

Figure 1.1: Drawing of a typical commercial condenser microphone (p is the acoustic pressure which causes a proportional movement in the membrane).

One alternative is to use inexpensive electret microphones. A drawing of a "back-electret" type of microphone is shown in Figure 1.2. The operating principle of the back-electret is very similar to the condenser microphone, with the primary distinction being the bonding of a permanently polarized electret material to the surface of the back-plate. This method of construction allows for the microphone to operate without a high-voltage power supply. While these have the advantage of being low-cost, electret microphones are known to vary widely with respect to mechanical/electrical sensitivity and phase. Also, the electret response tends to drift when exposed to environmental elements, and performance tends to degrade over time due to loss of surface charge [3].

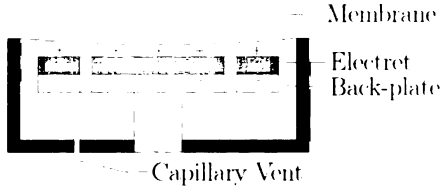

Figure 1.2: Drawing of a typical commercial electret microphone.

The utilization of micro-fabrication methods (microelectromechanical systems, or MEMS) to manufacture microphones based on known transduction methods (such as those described above as well as others) seems to hold promise in realizing mi-

crophones with the required dynamic range and bandwidth for aeroacoustics applications, while meeting the cost and response-matching requirements of beamforming arrays [4]. A systematic effort to realize this potential has been undertaken over the past few years by the Interdisciplinary Microsystems Group (IMG) at University of Florida. Some of the notable efforts of this group include the development of a MEMS piezoresistive microphone array [4], piezoelectric microphone [5], and dual-backplate condenser microphone [6],[7]. Other recent MEMS based microphones have been reported by [8], [9], and [10]. The device discussed in [8] uses a ZnO piezoelectric membrane and is tested as a microphone as well as a microspeaker. Optical interferometry using a diffraction-based grating has been incorporated for sensing of membrane displacement in [9] and [10].

The focus of the present thesis is a microphone concept alternative to those discussed above. The concept is that of a feedback-controlled microphone. In this approach, a feedback control loop is integrated into the sensor in order to detect and nullify the microphone's membrane deflection, caused by the sound pressure, using an opposing pressure that is produced by electrostatic, electromagnetic, or other electrical means. The presence of the feedback-control provision in the microphone provides a means by which to alter the microphone's dynamics, giving advantages for aeroacoustic beamforming measurements that are not attainable in conventional or MEMS-based microphones reported in the literature. For example, the feedback parameters can be tuned to adjust the microphone's bandwidth and dynamic range. This enables the same sensor to be employed in field testing at airports (where the bandwidth required is <20 kHz and maximum Sound Pressure Level (SPL) is less than 120 dB [5]) as well as in 1/4-scale model testing in anechoic wind tunnels (where the requirements are 50 kHz of bandwidth and maximum SPL exceeding 160 dB [5]). The tuning of control parameters can also be used to compensate for the modifying influence of

environmental factors (e.g. temperature, dirt and humidity) on the sensor's response. In fact, in the limit of sufficiently high feedback gain, the microphone's response is dominated by the dynamics of the feedback circuitry [11]. Thus, the response becomes independent of any environmental effects on the mechanical and electrical behavior of the membrane and deflection transduction scheme (capacitive, piezoresistive, etc). Finally, the actuation scheme used allows for "self-calibration" of the microphone without the necessity of an acoustic calibration setup. In turn, such capability holds the potential for "self-matching" of microphones in an array application.

1.2 Previous Feedback-Controlled Microphones

Previously, in [12], the response of a force-feedback microphone was evaluated. This microphone used electrostatic actuation of a pressure-gradient type microphone capsule. The feedback signal was based on modulation of an LC oscillator's frequency caused by the change in the microphone capsule's capacitance. In a follow-up study aiming to improve the design of the microphone, the *potential* and associated advantages for using a Fabry-Perot interferometer for the feedback sensor were investigated in detail, but no microphone prototypes employing the interferometer were constructed [13]. Overall the study lacked evidence demonstrating the advantages of feedback microphones (based on Figure 17 in the article).

Additional published material pertinent to feedback microphones include a patent for a force balance microphone that lists possible transduction and displacement detection methods, including optical methods [14]. The patent, however, only lists the microphone's concept without giving any experimental data regarding the response of an actual feedback microphone prototype. More recently, [15] developed a MEMS

based microphone that incorporates the displacement sensing method of [9] and [10] for measurement of a centrally hinged biomimetic membrane with electrostatic actuation in a feedback system. The construction of this MEMS sensor was motivated by hearing-aid applications, and thus the sensitivity response of the unit was highly non-uniform, which renders it unsuitable for aeroacoustic applications. No phase-response data were reported.

1.3 Description of Current Research

The uniqueness of the current study derives from the combination of actuation and sensing techniques that are being used for the first time to implement a feedback microphone. In particular, the microphone prototype constructed and characterized here integrates thin film PVDF (polyvinelidine-fluoride) as the pressure sensitive membrane. The actuation provision is naturally integrated into a microphone constructed in this manner by employing the piezoelectric properties of the PVDF. The simplicity of this construction relative to other feedback microphones reported in the literature is evident, given that no special means are necessary to construct the actuator (such as the back-plate in electrostatic or coils in electromagnetic actuation). In this regard, the current prototype has the potential to be simple and inexpensive to fabricate while satisfying the requirement for accurate sensor-response matching in an array application. This is particularly true since the present sensor concept is also amenable to construction using MEMS.

Two types of optical techniques are investigated for sensing of membrane displacement in the prototype microphones developed for this research; the fiber-optic lever and Michelson interferometer. Optical sensors are considered desirable for their in-

sensitivity to noise; hence decoupling the displacement sensor output from the influence of the actuator signal. The associated trade-offs in sensitivity, noise floor, frequency bandwidth, and linearity are discussed in evaluations of the two sensing techniques.

An integral part of this research is the mathematical analysis necessary for effective design of the control system. Foremost is development of a methodology for system identification and modeling the dynamics of the microphone membrane, optical sensor, and electrical components. These models are used in calculation of control parameters, where the closed-loop response is based on a set of user specified parameters corresponding to a desired microphone frequency response. Specifically, the research demonstrates that this two-step approach of modeling and control design is promising for "self-matching" of microphones in array where membranes with mismatched open-loop frequency response are forced to the same closed-loop response via feedback.

The first prototype microphone, described in Chapter 2, used a commercial fiber-optic lever sensor for measurement of the deflection of a 12.7mm diameter membrane. This prototype provided the basis for development and testing of modelling and control design of the optical feedback-controlled microphone system. In Chapter 3, results are reported on testing of a second prototype with a sensor diameter of 6.35mm. This sensor had the desirable properties of smaller size and higher frequency bandwidth. However, due to the inherent trade-off between membrane resonant frequency and mechanical sensitivity (i.e. m/Pa), the use of an optical sensor with much greater displacement sensitivity (i.e. V/m) was necessary. For this purpose, the Michelson interferometer setup was implemented. The knowledge gained from these two studies gave insight into potential design improvements for future prototypes. Chapter 4 gives

theoretical as well as experimental verification of two of these potential improvements, those being (1) an optical sensor that averages displacement over a large fraction of the membrane's area (both sensors used here detected the central displacement of the membrane), and (2) a perforated back-plate designed to increase damping of the mechanical resonances of the membrane. A summary of the findings is given in chapter 5, along with conclusions and future recommendations.

Chapter 2

A Novel Feedback-Controlled Optical Microphone using a Commercial Fiber-Optic Sensor

2-1 Microphone Construction and Feedback System Components

2-1-1 PVDF Film Microphone Capsule

A prototype microphone capsule with a membrane diameter of 12.7mm is constructed using a stretched PVDF membrane as the acoustic pressure sensing element as illustrated in Figure 2.1. The capsule body and clamping ring are constructed from aluminum rod. The membrane, which is metallized with an aluminum layer on both sides, is clamped between the body and ring with a rubber gasket air seal. In this way,

the body and ring apply tension to the membrane, and also act as electrical conductors to the metallized surface of the PVDF film. At the end opposite to the membrane, an acrylic plate is attached to the capsule body with a rubber gasket inserted in between. The gaskets prevent air leakage from the internal cavity of the microphone capsule, enabling pressurization of the capsule for reasons that will become clear. The pressurization is achieved through a static pressure tap that is installed in the acrylic plate. The tap couples, via a T connection, to a syringe as well as a pressure gage, allowing variation and monitoring of the internal static pressure.

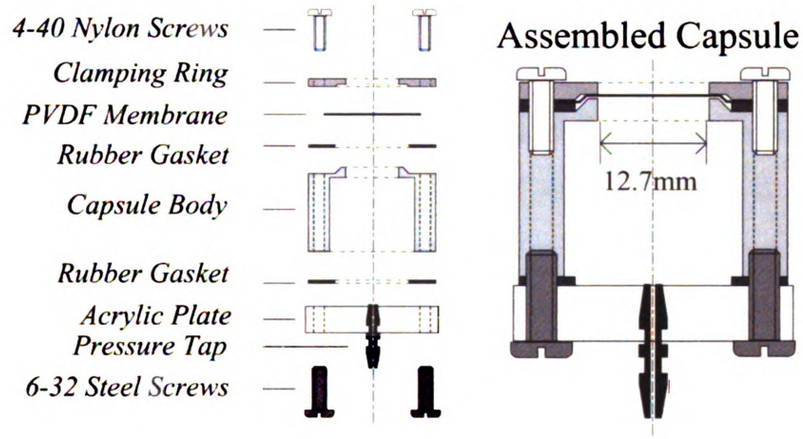

Figure 2.1: Schematic drawing of prototype microphone capsule: exploded (left) and assembly (right) views.

The piezoelectric properties of the PVDF can be exploited to electrically induce deflection of the membrane surface. This is important for two reasons, (1) the membrane can act as an actuator in a feedback loop, and (2) the transfer function and thus frequency response of the membrane can be determined through electrical actuation, without the necessity of an acoustic calibrator. It is well known that the response of a PVDF membrane while being actuated in this manner (i.e. deflection per unit voltage applied across the top and bottom surfaces) is greatly increased when it has some curvature as opposed to being flat [16], [17], [18]. For convenience, this is achieved in

the current prototype by applying static pressurization using the provisions described above. Of course, although this method is suitable for laboratory characterization of prototypes, construction of commercially viable sensors will ultimately have to employ a more practical approach by inducing curvature either through a material treatment or alternate mounting methods. For example, a self-supporting, dome-shaped piezoelectric structure can be manufactured by applying an electric field across the film while stretched over a steel sphere at temperatures of 80°C, as described by [17].

2.1.2 Fiber-Optic Lever Displacement Sensor

An optical sensor is used to measure the deflection of the membrane in response to incident acoustic pressure. The particular type of sensor employed is a fiber-optic lever, model Philtec D20. When aimed at a reflective surface, light emitted from a transmitting fiber is reflected back into bundled receiving fibers, and is detected by a photodetector. Thus, the output of the photodetector will be a function of the separation distance between the probe tip and the reflective surface [19]. A sensor using this setup and seven optical fibers is depicted in Figure 2.2. In the case of the sensor used for this research, output voltage increases linearly with the gap size between the probe tip and the membrane. Its linear operation is sustainable over a maximum displacement of 23μm and frequency bandwidth of 20 kHz with a typical sensitivity of 86mV/μm. The latter is obtained from calibration using a stationary target prior to taking measurements.

The fiber-optic lever sensor is aimed at the center of the PVDF membrane. The combination of these two components (i.e. sensor and membrane) define the open-loop operation of the microphone, where the output voltage of the optical sensor is a function solely of the acoustic pressure acting on the membrane and the membrane

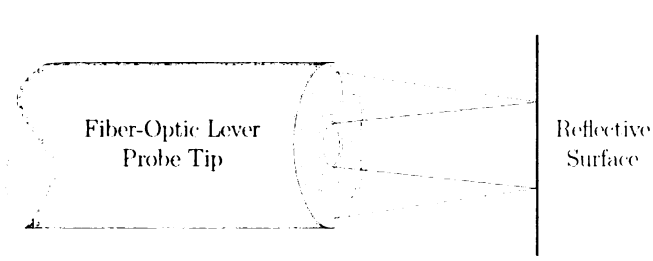

Figure 2.2: Schematic drawing of fiber-optic lever probe.

and lever sensor dynamics. Without the feedback, this setup is similar in nature to the optical microphones reported in [20] and [21].

2.1.3 Feedback System Components

The aim of this work is to demonstrate the closed-loop operation of the sensor where the microphone dynamics are modified by a feedback control system as depicted by the block diagram in Figure 2.3. The two additional blocks that describe the sensor's response in closed-loop operation are the compensator and piezoelectric system. The compensator is constructed using operational amplifiers, and its transfer function is set by precision trim-pots. The piezoelectric system consists of a piezo driver and the membrane itself. The piezo driver used is a ThorLabs model MDT694 which provides a gain factor of 15 for input voltages in the range of 0-10V. Calibration has been performed to show that the unit has a bandwidth of 140kHz with a transfer function similar to that of a second-order, slightly under-damped, low-pass filter. Voltage from the piezo driver in conjunction with the piezoelectric properties of the membrane induce an electrical equivalent pressure that acts in opposition to the acoustic pressure. This provides the basis for negative feedback.

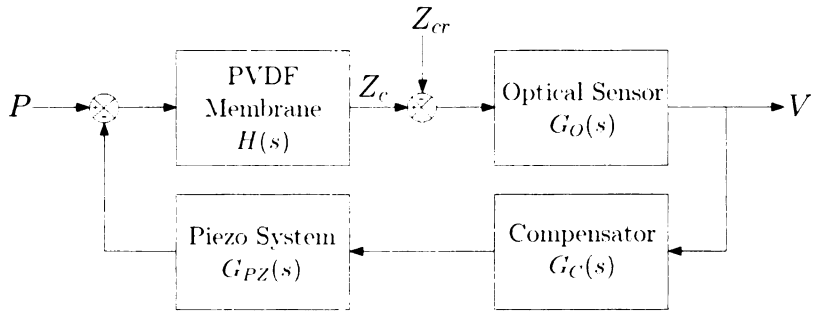

Figure 2.3: Control block diagram for optical feedback controlled microphone system. Note that P, Z_c, Z_{cr} and V are the Laplace transforms of the acoustic pressure, actual and reference central membrane deflection, and output voltage respectively.

2.2 Analytical Modeling

The transfer function relating the voltage output (V) of the optical sensor to acoustic pressure input (P) for the closed-loop system depicted in Figure 2.3 is given by equation (2.1) below. Here, $H(s)$ represents the membrane transfer function, while $G_O(s)$, $G_C(s)$, and $G_{PZ}(s)$ represent the optical sensor, compensator, and piezoelectric system respectively, each modeled in the Laplace domain. This provides the basis for analytical design and prediction of the frequency response of the closed-loop system.

$$\frac{V(s)}{P(s)} = \frac{H(s)G_O(s)}{1 + H(s)G_O(s)G_C(s)G_{PZ}(s)} \tag{2.1}$$

The physical plant in the control system is the membrane. For small displacements, that are typical in response to acoustic excitation, it is suggested by [22] that the membrane deflection can be modeled by the linear wave equation for a stretched membrane, given in equation (2.2), with T, $z(r,\theta,t)$, $p(r,\theta,t)$, and ρ_s representing membrane tension, displacement, acoustic pressure, and surface density, respectively,

r and θ are polar coordinates in the plane of the membrane before deflection, t is time and ∇^2 is the laplacian operator.

$$T\nabla^2 z + p = \rho_s \frac{\partial^2 z}{\partial t^2} \tag{2.2}$$

In the optical microphone system, displacement is measured at the center of the membrane, represented by z_c. A simple approximation for the fundamental (lowest order) resonant mode of the system can be made by assuming the membrane to undergo axi-symmetric, parabolic deflection. This yields equation (2.3), where a is the membrane radius:

$$\rho_s \ddot{z}_c + \frac{4T}{a^2} z_c = p \tag{2.3}$$

This equation is then transformed into the Laplace domain, where $M = \rho_s$, $K_0 = 4T/a^2$, and a generalized damping term C_0 is added. Thus, the transfer function relating the center displacement to the acoustic pressure is given by:

$$H(s) = \frac{Z_c(s)}{P(s)} = \frac{1}{Ms^2 + C_0 s + K_0} \tag{2.4}$$

In developing the membrane transfer function, it is assumed that the mass term, M, is fixed, and is known from the PVDF film's thickness and volume density. The stiffness and damping terms are identified from calibration of the membrane's frequency response using electrical actuation of the piezoelectric membrane. Since the membrane tension T is difficult to directly determine, the stiffness term K_0 is identified based on the observed fundamental resonant frequency ω_0 using:

$$K_0 = \omega_0^2 \rho_s \tag{2.5}$$

The damping ratio ζ_0 for the highly underdamped system is identified using equation (2.6), where ω_H and ω_L are the half-power frequencies located on each side of the resonant frequency ω_0.

$$2\zeta_0 = \frac{\omega_H - \omega_L}{\omega_0} \tag{2.6}$$

This allows for the damping C_0 to be calculated as follows:

$$C_0 = 2\zeta_0 \sqrt{M K_0} \tag{2.7}$$

In practice, multiple resonant peaks are observed at the frequencies predicted for the axi-symmetric modes of the circular membrane. These peaks were determined to be a cause of instability in the feedback system, and thus were accounted for in the transfer function. A modified membrane transfer function is presented in equation (2.8) below with $C_m = (\omega_m/\omega_0)^2 C_0$, $K_m = (\omega_m/\omega_0)^2 K_0$, and ω_m/ω_0 representing the resonant frequency ratios for the higher order modes calculated from membrane vibration theory, and tabulated, for example, in [23].

$$H(s) = \frac{Z_c(s)}{P(s)} = \sum_{m=0}^{N-1} (-1)^m \frac{1}{Ms^2 + C_m s + K_m} \tag{2.8}$$

Note that N is the number of modes retained in the model. Here five modes are used because these appear in the calibration frequency range. Also, The factor $(-1)^m$ in

equation (2.8) is required to obtain the proper phase behavior. To clarify, consider summing two second-order systems to model the leading two resonant frequencies of the membrane. In the limit of infinite frequency, the phase angle of the transfer function of each of the two systems composing the model asymptotes to 180 degree. The summation of two complex numbers with 180 degree phase also has a phase of 180 degree. Experimentally, the phase angle experiences 180 degree phase change at every resonance frequency. Thus, for the two-resonant-frequency system, the phase angle should asymptote to 0, and hence the transfer functions should be subtracted rather than added.

Once equation (2.8) has been determined for the microphone being tested, the compensator $G_C(s)$ is designed to achieve a desired closed-loop frequency response. This is done using a pole placement method as described by [24]. The compensator used is phase lead, and has a transfer function given by equation (2.9), where a_1, a_0, and b_1 are phase-lead parameters to be calculated. K_p, K_d, and τ_d represent the compensator's proportional gain, derivative gain, and derivative time constant. The electrical circuit employed to implement this controller is shown in Figure 2.4. Design equations for the circuit are given in Table 2.1.

$$G_C(s) = \frac{a_1 s + a_0}{b_1 s + 1} = K_p + \frac{K_d s}{\tau_d s + 1} \tag{2.9}$$

The closed-loop system has a third-order characteristic equation (denominator of equation 1). To tune the close-loop response to that desired, two of the roots of the characteristic equation are set to correspond to a complex pole s_1. The location of this pole, defined by equation (2.10) in terms of polar coordinates, is set as desired in the left half of the complex plane and has a magnitude $|s_1|$ and angle β relative to

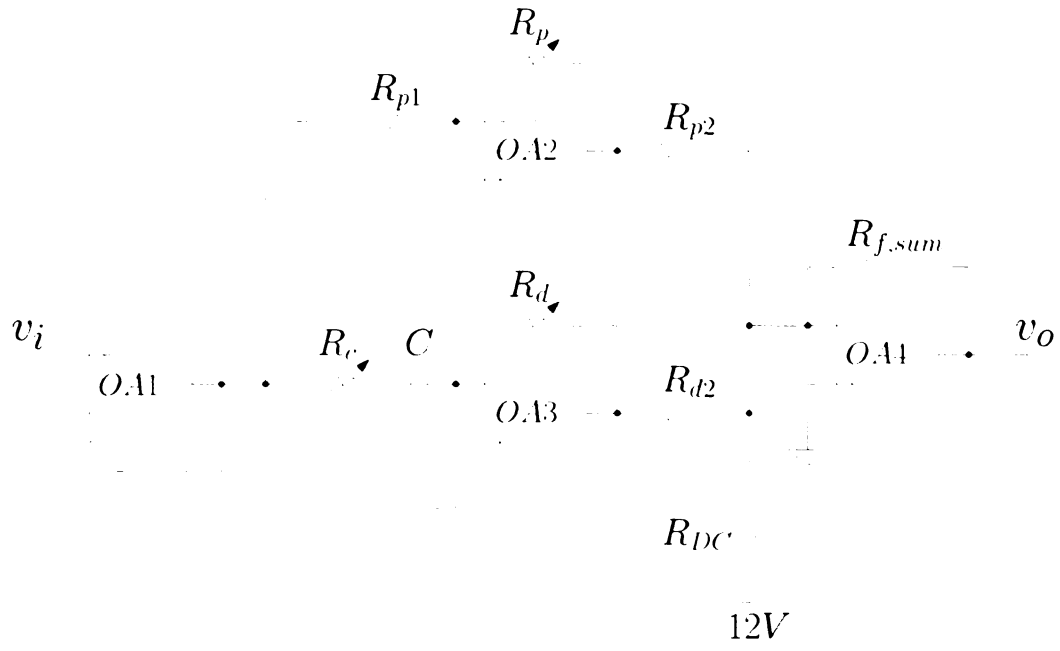

Figure 2.4: Schematic diagram of circuit used for implementation of the phase-lead compensator.

the positive real axis. Both of these quantities are related to the desired closed-loop fundamental resonance frequency $\omega_{0,CL}$ and damping $\zeta_{0,CL}$ as given by equations (2.11) and (2.12).

$$s_1 = |s_1|e^{j\beta} \tag{2.10}$$

$$\omega_{0,CL} = |s_1| \tag{2.11}$$

$$\zeta_{0,CL} = -\cos\beta \tag{2.12}$$

This pole is plugged into the system's characteristic equation as shown:

Table 2.1: Design equations for compensator circuit. Resisters are represented by $R_{p1}, R_{p2}, R_{d2}, R_{DC}$ and, $R_{f.sum}$, while potentiometers R_p, R_c, R_d control proportional gain, derivative time constant, and derivative gain. A fixed capacitance is represented by C.

Parameter	**Equation**
Proportional Gain	$K_P = \frac{R_p R_{f.sum}}{R_{p1} R_{p2}}$
Derivative Gain	$K_d = \frac{R_d R_{f.sum} C}{R_{d2}}$
Derivative Time Constant	$\tau_d = R_c C$
DC Bias	$V_{DC} = 12V \frac{R_{f.sum}}{R_{DC}}$

$$1 + H(s_1)G_O(s_1)G_C(s_1)G_{PZ}(s_1) = 0 \tag{2.13}$$

Letting $H(s_1)G_O(s_1)G_{PZ}(s_1) = |H(s_1)G_O(s_1)G_{PZ}(s_1)|e^{j\psi}$ equation (2.13) can be solved for $G_C(s_1)$ to yield equations (2.14) and (2.15) for the controller parameters a_1 and b_1.

$$a_1 = \frac{\sin\beta + a_0|H(s_1)G_O(s_1)G_{PZ}(s_1)|\sin(\beta - \psi)}{|s_1||H(s_1)G_O(s_1)G_{PZ}(s_1)|\sin\psi} \tag{2.14}$$

$$b_1 = \frac{\sin(\beta + \psi) + a_0|H(s_1)G_O(s_1)G_{PZ}(s_1)|\sin\beta}{-|s_1|\sin\psi} \tag{2.15}$$

Note that a_0 in the above equations can be computed based on the desired DC response of the closed loop. More specifically, the latter is given by:

$$\frac{V(\omega \to 0)}{P(\omega \to 0)} = \frac{S_H S_O}{1 + S_H S_O S_C S_{PZ}} \tag{2.16}$$

where each the S terms in equation (2.16) represent the DC sensitivity of the corresponding system, and they are all known except S_C. Realizing that $S_C = a_0$ (see equation (2.9)), it is then possible to calculate a_0 based on a desired DC response (or attenuation).

2.3 Experimental Procedure

The two primary experiments conducted are calibration of the microphone using electrical actuation, followed by calibration of the microphone's acoustic response in a plane wave tube (PWT). Electrical actuation is used as a means of identifying open-loop membrane parameters based on its measured frequency response (using equations (2.5) through (2.7)). These parameters are subsequently applied using the method described at the end of section 2.2 to the design of the system's compensator. Calibration in the plane wave tube is then undergone to verify that the actual frequency response for both open- and closed-loop operation conforms to predictions based on the theoretical model.

In the electrical actuation calibration, a Hewlett-Packard 33120A function generator is used to produce a harmonic sweep waveform over the frequency range 10Hz-25kHz. This waveform is input to the piezo driver, while simultaneously being recorded using a PC-based, National Instruments PCI-6024E, 12-bit Analog-to-Digital converter. The piezo driver provides a voltage gain factor of 15 producing an amplified output that is applied across the electrodes of the PVDF film membrane. Membrane deflection is simultaneously measured by the fiber-optic lever sensor. The resulting data are used to obtain the frequency response relating the membrane displacement to the applied voltage from:

$$H_{act}(\omega) = \frac{\phi_{vz}(\omega)}{\phi_{vv}(\omega)} \tag{2.17}$$

where ϕ_{vz} is the cross-spectrum between the input voltage to the piezo driver and the membrane's deflection, and ϕ_{vv} is the auto-spectrum of the former. In this test, 8,192,000 data points are recorded at a sampling frequency of 50kHz. To obtain the spectra, the time series were broken into 2000 records, and the spectra obtained from the individual records were averaged resulting in a random uncertainty of 2.24%.

The microphone is placed inside the PWT which acts as an acoustic waveguide in which sound propagates as plane waves up to a cutoff frequency based on the tube's cross-sectional dimensions. The tube used for this experiment has a square cross-section with a side length of 31.75mm resulting in a cutoff frequency of approximately 5kHz (which corresponds to an acoustic wavelength of twice the side length [23]). The test microphone is mounted in the plane wave tube at the same cross section as a B&K type 4938A 1/4" reference microphone with known manufacturer calibrated response. This configuration ensures that the microphone under test will be subjected to equal acoustic pressure and phase as the reference microphone. The probe tip of the fiber-optic lever sensor is placed inside the plane wave tube and aimed at the center of the membrane. Fine positioning of the probe is performed using a translation stage with 0.2 μm precision. A schematic drawing of the plane wave tube showing positioning of the test microphone, reference microphone, and optical sensor is shown in Figure 2.5. It is noted here that this "external" placement of the optical sensor is employed for convenience, and is suitable for testing of prototypes. However, in practical microphones, the optical fibers would be integrated into the microphones capsule, and aimed at the back of the membrane.

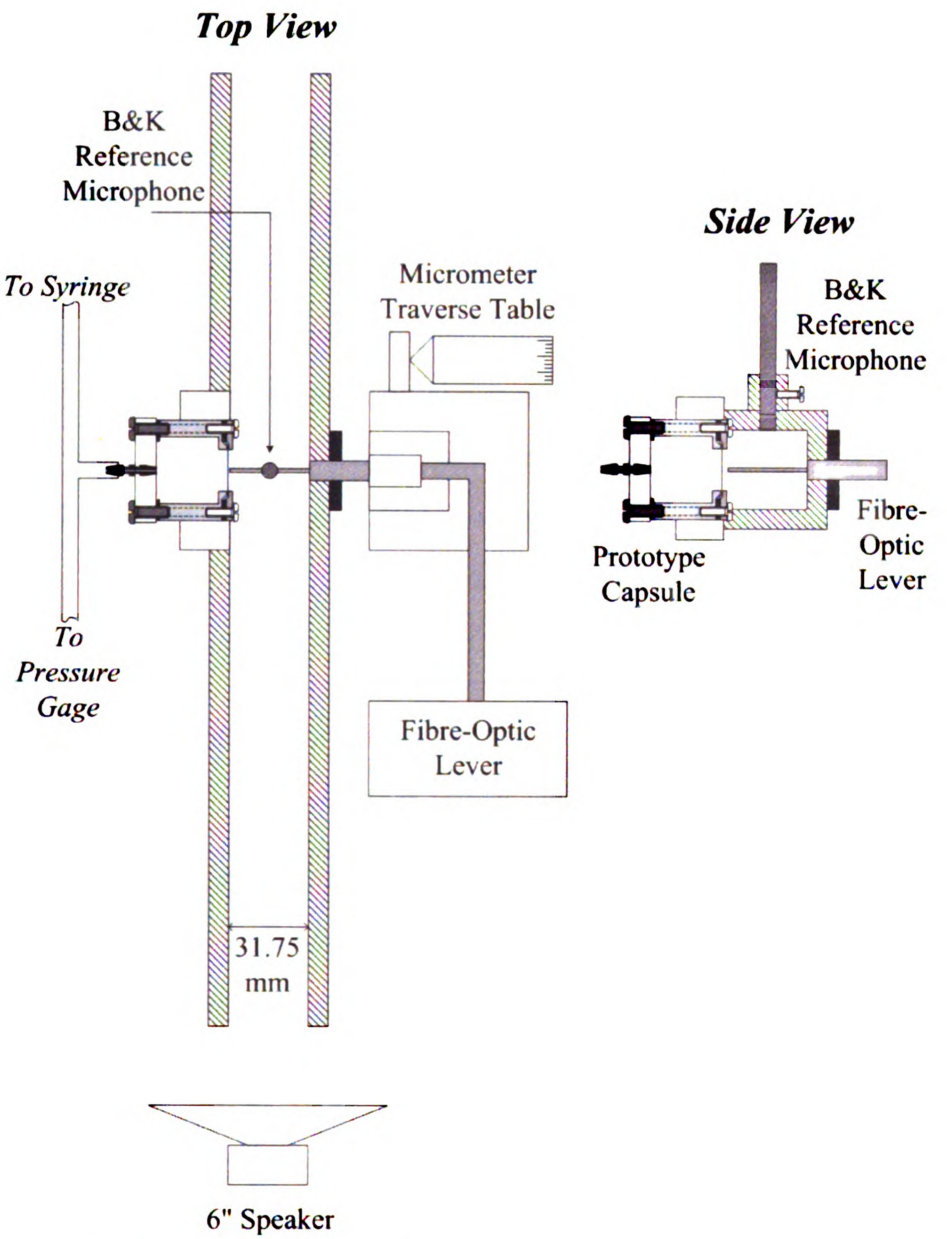

Figure 2.5: Schematic diagram of the plane wave tube calibration setup.

For the acoustic calibration, a Hewlett-Packard 33120A function generator is used to supply white noise signal to a Dayton RS150S-8, 40 Watt speaker that is powered by Hafler P1000, 110 Watt amplifier. The sound produced by the speaker excites the plane wave tube. The output signal from the B&K reference microphone and the fiber-optic lever sensor are recorded at a sampling rate of 50kHz for a total of 4,096,000

samples. The same analysis procedure described above for obtaining the electrical-actuation response is applied to these signals to obtain the acoustic response, with the additional provision that the phase response of the reference microphone must be subtracted to yield absolute phase. Two acoustic calibration tests are conducted. First, the acoustic response of the prototype microphone is measured in open-loop operation to verify that its response conforms to that predicted by the parameters identified in electrical actuation. Next, the microphone system is operated in closed-loop mode, and the response is measured. Observation of the frequency response in open- and closed-loop operation is used to validate the theoretical model.

2.4 Results and Discussion

Initially, a set of tests were performed to characterize the change in electrical actuation sensitivity (S_{act}) for variations in internal static pressurization. The results of these tests are shown in Figure 2.6. The figure shows two plots: one depicts the change in S_{act} with pressure (top plot), and the other gives the corresponding membrane's resonance frequency f_0 (bottom plot). The latter is included since it is anticipated that the increase in internal pressure will increase the membrane's tension, and hence the resonance frequency as well. As mentioned previously, it is expected that the induced curvature of the membrane will result in an increase in the actuation sensitivity, obtained here from the average membrane displacement per unit applied voltage at frequencies well below resonance. This is consistent with the data in Figure 5 which shows significant increase in actuation sensitivity, from 1.87 nm/V for the un-pressurized case, up to 16.8 nm/V at 3.2kPa. Similarly, the fundamental resonance frequency is raised from 3.61 kHz at 0kPa to 4.06 kHz at 3.2kPa.

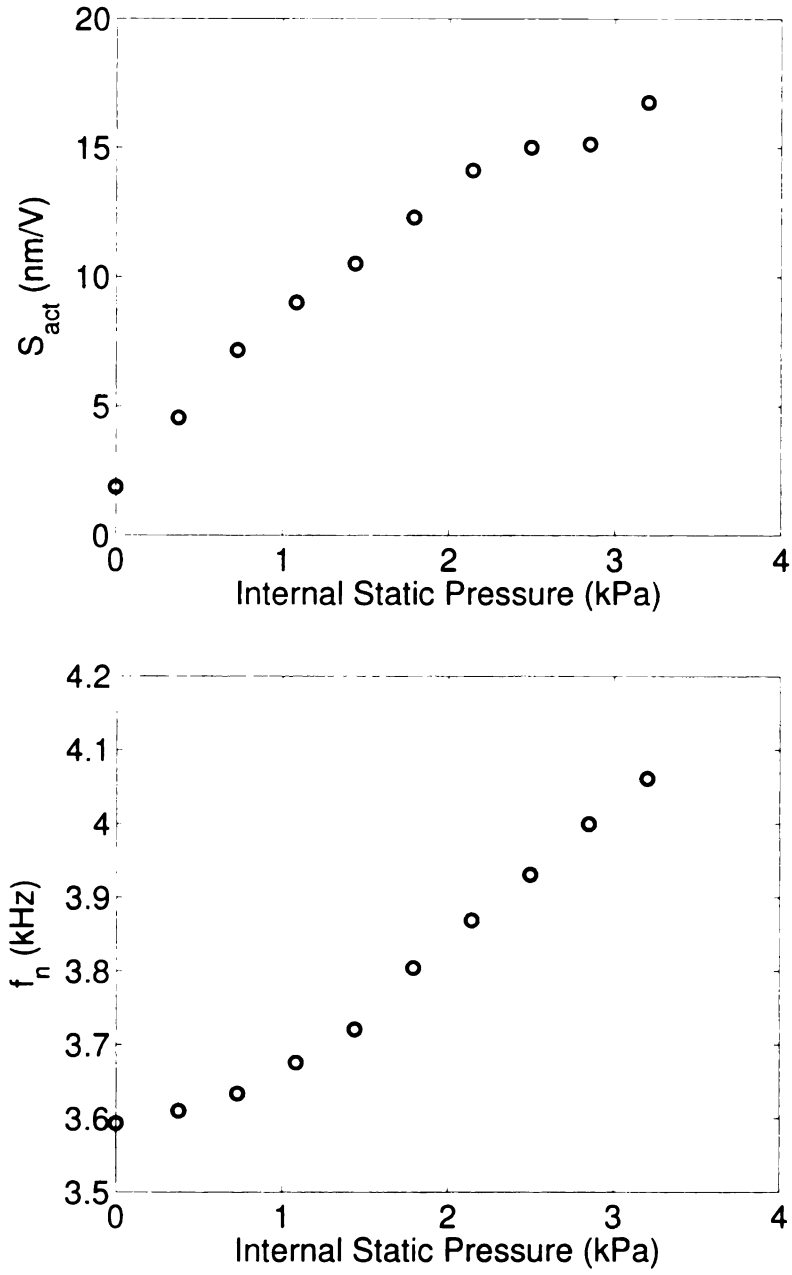

Figure 2.6: Electrical response of PVDF membrane for variation of internal static pressurization: (top) actuation sensitivity of PVDF membrane; (bottom) fundamental resonance frequency of PVDF membrane.

From the static pressurization results, an internal static pressure of 1.5kPa is chosen for further testing as this provides the desired increase in actuation sensitivity without significantly affecting the characteristics of the membrane from its un-pressurized

condition. An electrical calibration of the membrane for the selected internal pressure is shown in Figure 2.7 across a 100Hz-25kHz bandwidth. The calibration is compared to the analytical membrane model given by equation (2.8). Good agreement is seen between the predicted and measured membrane's response. This indicates that the model employed is effective in capturing the resonant peaks of the membrane, though there is some deviation that is believed to be caused by acoustic reflections inside the PWT (note that the electrical calibration is conducted while the microphone is mounted in the PWT in order to maintain the same conditions for both electrical and acoustic calibrations). Open-loop parameters identified using the electrical calibration in Figure 2.7 are given in Table 2.2, where the stiffness and damping terms refer to those identified for the fundamental resonant mode of the membrane.

Table 2.2: Microphone parameters for open-loop operation

Parameter	**Symbol**	**Value**	**Unit**
Mass	M	0.049	kg/m^2
Damping	C_0	15.9	$Pa \cdot s/m$
Stiffness	K_0	$26.2 \cdot 10^6$	Pa/m
Damping Ratio	ζ_0	$7.42 \cdot 10^{-3}$	
Natural Frequency	f_0	3.61	kHz
Microphone Sensitivity	S_M	3.58	mV/Pa

After the system parameters are identified using electrical actuation, acoustic testing is performed using the PWT. Initially, the microphone is tested in open-loop mode to verify the analytical model and to provide a base-line reference for comparison to closed-loop mode. Then, the closed-loop system's DC attenuation and complex pole location are specified. Following the procedure outlined at the end of section 2.2, a MATLAB design program is used to calculate the compensator transfer function required to achieve the user specified parameters, and outputs corresponding values for the phase-lead circuit (shown in Figure 2.4). Figures 2.8 and 2.9 show the frequency response up to the PWT cutoff of 5kHz of two different closed-loop implementations

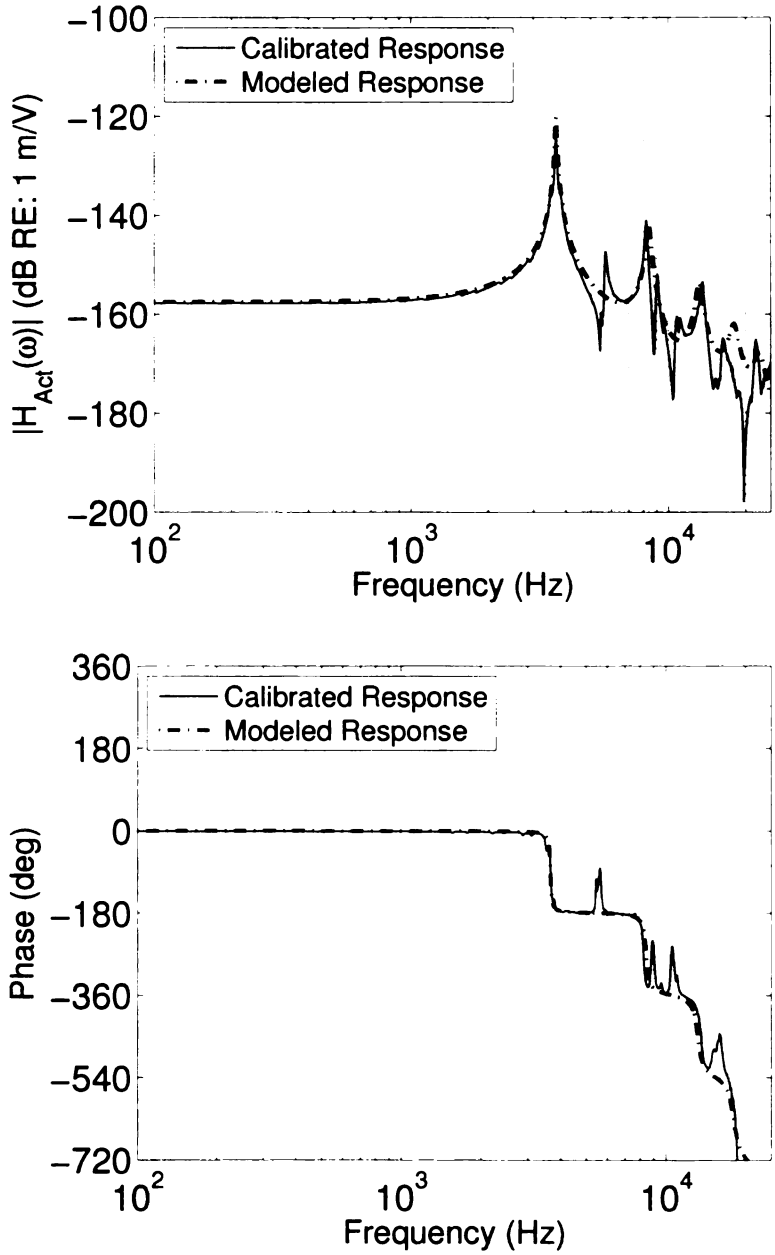

Figure 2.7: Frequency response of PVDF membrane identified using electrical actuation with 1.5kPa internal pressurization: (top) Actuation sensitivity of PVDF membrane; (bottom) Phase response of PVDF membrane

of the same microphone capsule. The frequency response predicted by the analytical model for each implementation is also shown on the same plot over a frequency range exceeding the cutoff frequency of the PWT.

The implementation shown in Figure 2.8 targets an increase in resonant frequency and damping with 0dB DC attenuation (i.e. without affecting the microphone's sensitivity). As seen from the figure, the fundamental resonant frequency has been increased from 3.61kHz in the open-loop system to the design frequency of 5.1kHz in the closed-loop system, corresponding to a 41% increase in bandwidth as a result of feedback. Most important, however, is the effectiveness of the analytical model in predicting the closed-loop response, which is a primary aim of the current work with potential applications in "self-calibration" or "self-matching" of sensor parameters in beamforming arrays, as well as for tuning the microphone's response to match the needs of different applications (e.g. full-scale versus 1/4-model scale airframe noise testing).

The second result, shown in Figure 2.9, is for a design that specifies 3dB DC attenuation in addition to corresponding increase in resonant frequency. An increase of DC attenuation, or "stiffening" of the membrane, is desirable if the microphone is to be used for measurement of high SPL as it would result in improved linearity of the sensor.

Finally, the sensor's linearity and noise floor were determined for open-loop in addition to closed-loop operation (where the latter was operated at conditions similar to those of Figure 2.9). A sinusoidal sound at 1kHz was employed to drive the PWT. Power spectrum analysis was then used to measure the rms voltage output of the prototype and reference microphone at 1kHz for different sound levels. For each sound level, 25 averages were taken with a sampling frequency of 50kHz and a bin width of 1Hz to avoid spectral leakage (since the 1 kHz bin in the power spectrum analysis is an integer multiple of the bin width). The results are shown in Figure 2.10, where the rms output of the prototype sensor is plotted versus the sound pressure level

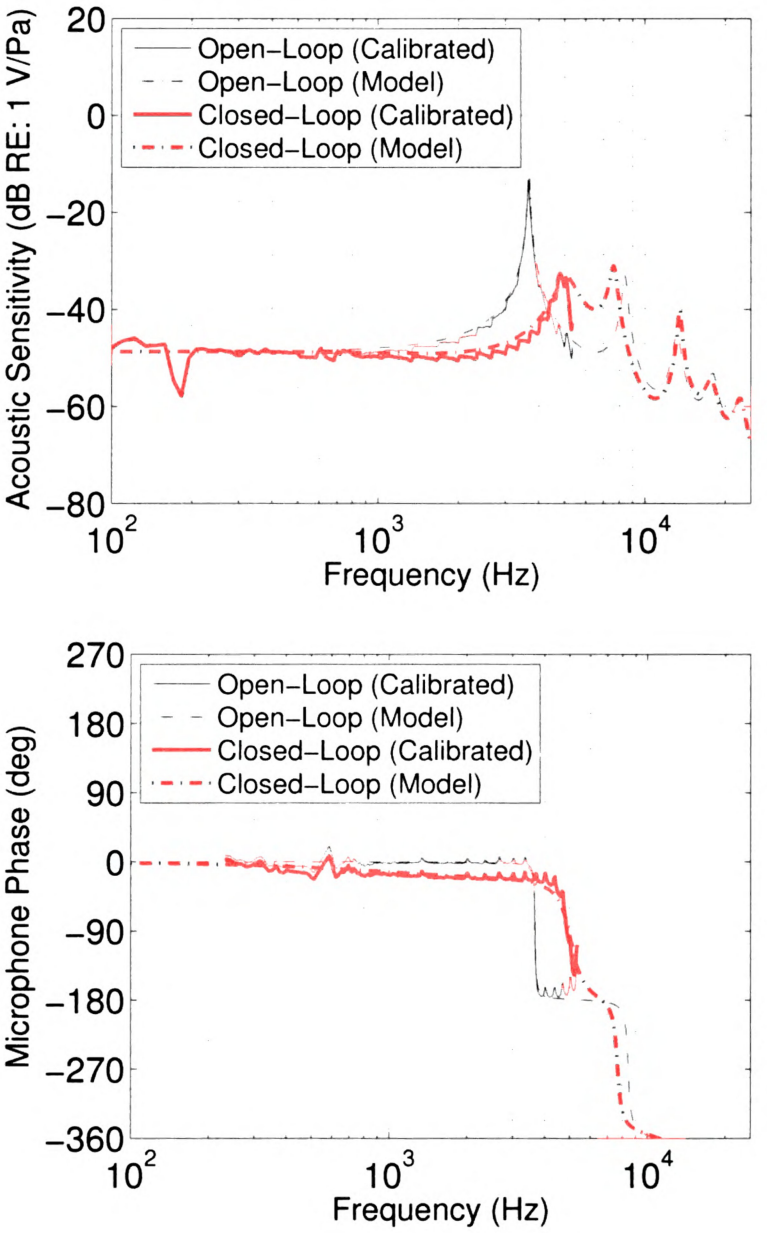

Figure 2.8: Response of microphone in open-loop and closed-loop operation for the design specification of 0dB attenuation, β=95°, and $f_{0,CL}$=5.1kHz: (top) acoustic sensitivity; (bottom) phase

recorded by the B&K microphone. As seen from the figure, the sensor demonstrates linear operation up to approximately 105dB, which was the limit of sound intensity produceable by the speaker and amplifier used. The maximum SPL for linear opera-

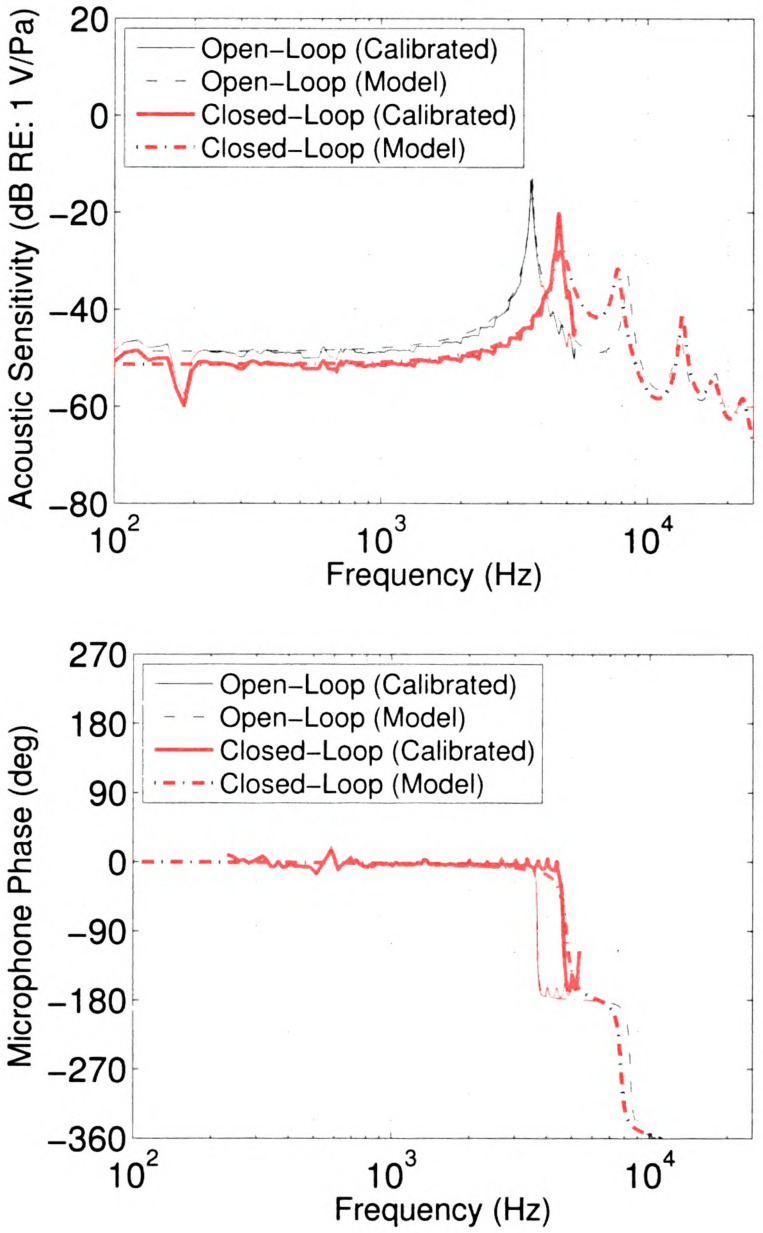

Figure 2.9: Response of microphone in open-loop and closed-loop operation for the design specification of 3dB attenuation, β=92.5°, and $f_{0,CL}$=4.8kHz: (top) Acoustic sensitivity; (bottom Phase

tion is clearly beyond the testing range. The corresponding sensitivity obtained from linear fit to the data in Figure 2.10 are 3.58 mV/Pa and 2.61 mV/Pa for open-loop and closed-loop operation, respectively. The noise floor is determined by measur-

ing rms voltage of the prototype sensor with the speaker turned off. The effect of this noise floor is clearly seen in the plot as a "flattening" of the sensor response at low SPL, where the noise signal is dominant. The observed rms voltages were 3.38 μV and 3.52 μV corresponding to noise floors of 33.5dB in open-loop and 36.6dB in closed-loop operation.

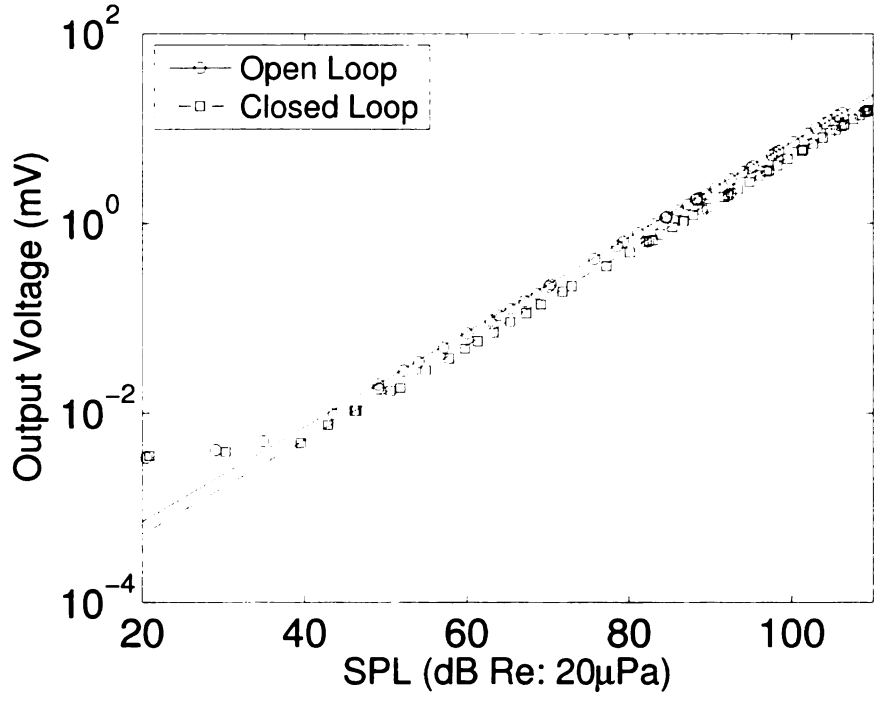

Figure 2.10: Linearity and noise floor for open- and closed-loop operation.

For both closed-loop implementations here, the effective controllability of the microphones, for example using higher values of K_p or K_d (see equation (2.9)) than those employed for the cases demonstrated here, is limited by instability that arises as an effect of higher order resonances. This can be considered to be a consequence of the relative simplicity of the phase-lead controller compared to the membrane model with its multiple resonances. Thus, it may be possible to achieve greater increases in closed-loop bandwidth or DC attenuation using more sophisticated control methods. Alternatively, the effect of the higher-order resonances can be substantially dimin-

ished through the use of mechanical damping means (such as the perforations in the back-plate of condenser microphones), and/or the use of an optical sensor that measures the average, rather than the central, displacement of the membrane. The latter helps in the sense that, unlike the fundamental resonance mode where the entire membrane is moving in phase, higher-order resonances involve movements where parts of the membrane are moving upwards while others are moving downwards. Thus, the average of this motion will be much smaller than the central displacement, and the influence of higher-order resonances on the optical sensor output will be substantially reduced.

Chapter 3

A Feedback-Controlled Optical Microphone Incorporating a Michelson Interferometer

In Chapter 2, a microphone was discussed that incorporated a fiber-optic lever displacement sensor for measurement of the deflection of the microphone's membrane. The sensor was commercially manufactured and proved simple to use in the development of a prototype microphone. However, a microphone prototype is desired with a frequency bandwidth that is wide enough to cover the entire human audible range of up to 20kHz. One effective method for increasing the bandwidth of a microphone is to decrease the diameter of the membrane. In fact, assuming surface mass density and membrane tension to be constant, halving the diameter of a membrane will double the resonant frequency as the membrane stiffness (Pa/m) is increased by a factor of four. For this purpose, a membrane prototype having a 6.35mm diameter membrane was fabricated. For convenience, this prototype is physically integrated into the

plane wave tube to be used for acoustic calibration. Because of the inherent trade-off between stiffness of the microphone membrane and measurement bandwidth, it is necessary that the optical sensor used with this smaller prototype have a higher sensitivity and lower noise floor than the fiber-optic lever sensor. The sensor technology implemented in this study is the Michelson interferometer.

3.1 Construction

3.1.1 Microphone Membrane

To satisfy the desired smaller sensor size and higher bandwidth a 6.35mm diameter microphone membrane was fabricated. While the construction of the new prototype does share certain common characteristics with the version described in Chapter 2, there are some notable differences which will be described.

Similar to the earlier prototype, the membrane is constructed from PVDF, in this case 28 μm thick uni-axial PVDF purchased from Measurement Specialties[1]. The film membrane is stretched and clamped between conductive electrodes, as done previously. In the newer prototype, the bottom electrode is a copper insert that has been embedded in an acrylic base plate, as seen in Figure 3.1. One notable difference in this design is that the high voltage copper electrode is isolated from the outside, which is important for safety purposes. A rubber O-ring is fitted around the copper electrode, which acts as a compliant surface providing friction to hold the membrane in place. The top electrode is an aluminum plate which has been attached to the acrylic plate using screws. This top electrode is electrically grounded. In order to

[1] `http://www.meas-spec.com/downloads/Piezo_Film_Product_Guide.pdf`

isolate the back side of the membrane from outside acoustic pressure, a second acrylic plate is attached using nuts to plug the back-chamber of the microphone.

The prototype discussed in Chapter 2 was acoustically calibrated up to the plane wave tube cutoff frequency, which was approximately 5.3 kHz. Since a higher bandwidth is expected with the 6.35mm prototype, a PWT calibration setup was desired with a higher cutoff frequency. For this purpose, a channel was milled from acrylic with a side width of 7.9mm. When this channel is screwed to the plate upon which the microphone membrane is mounted, it forms a plane wave tube with a cutoff frequency of approximately 21 kHz. Top and side views of the prototype and plane wave tube calibrator are shown in Figure 3.1 while a front view is shown in Figure 3.2.

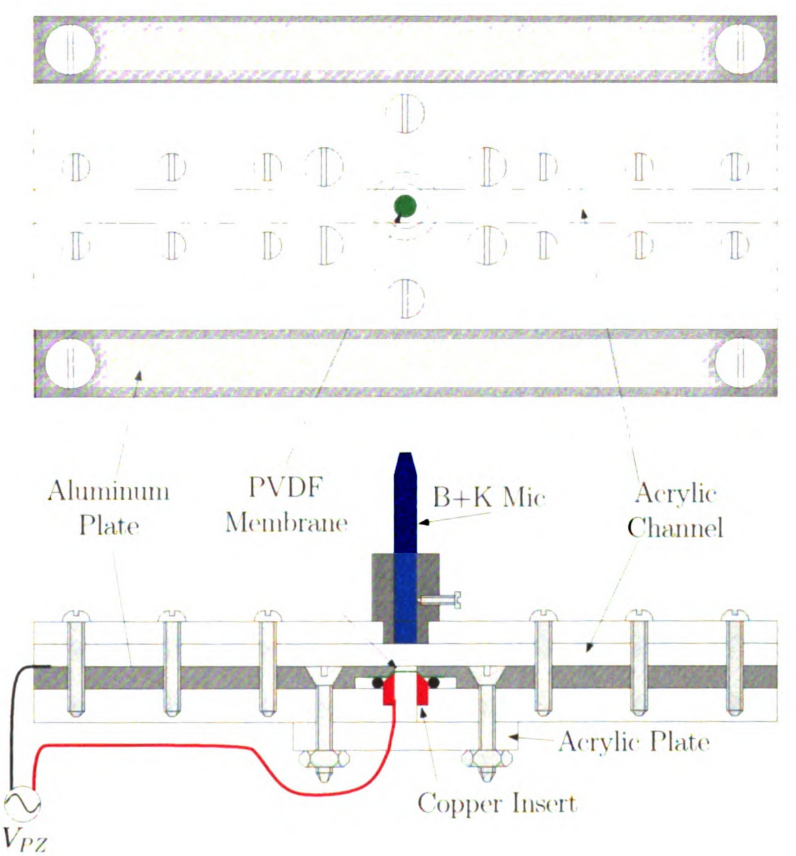

Figure 3.1: Depiction of 6.35mm diameter membrane prototype, top: top view, bottom: side view.

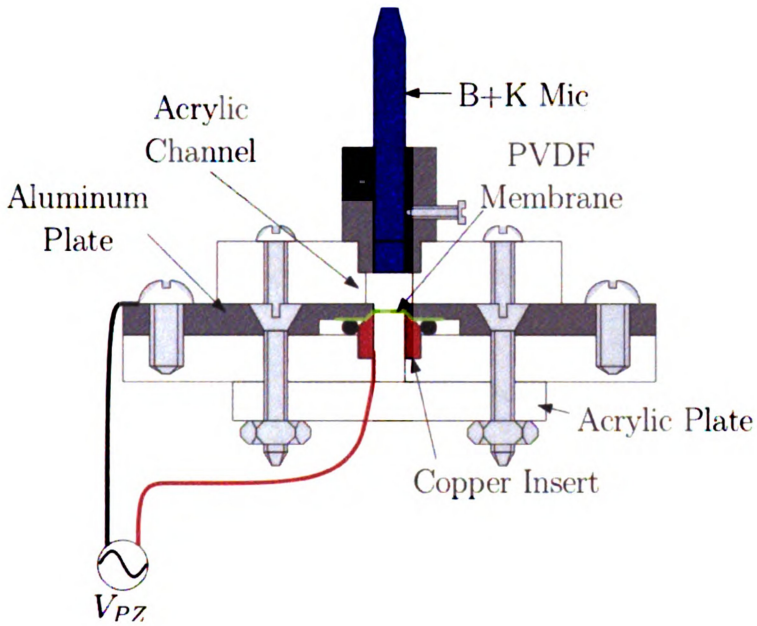

Figure 3.2: Front view depiction of 6.35mm diameter membrane prototype with acrylic channel (PWT) attached.

3.1.2 Michelson Interferometer

The interferometer displacement sensor used here is implemented on an optical table. Though such implementation is not suitable for realizing compact and practical microphones, it works well for the purposes of proof of concept and prototype characterization. Future integration of the interferometer in practical sensors can be accomplished using fiber optics. A schematic representation of the common Michelson interferometer is shown in Figure 3.3, while a photograph is shown in Figure 3.4. The setup used for this experiment uses a Uniphase Model 1135P He-Ne laser with an optical wavelength of 633nm and total output power of 20mW. The polarized and collimated output from the laser initially passes through a $\lambda/4$ plate to prevent reflected light from returning into the laser cavity. This beam then passes through a 50/50 beam-splitter (BS) where it is separated into signal and reference arms. The signal arm is aimed at the center of the microphone membrane and is reflected back

to the beam-splitter before being directed through a focusing lens to a ThorLabs DS110 photodetector, which has a sensitivity of 0.4 A/W at the 633nm wavelength. The reference arm is reflected off a mirror that is mounted on a piezoelectric stack (PZ Mirror). The two beams are combined at the photodetector where the measured optical intensity is a sinusoidal function of the difference in phase between the signal and reference arms.

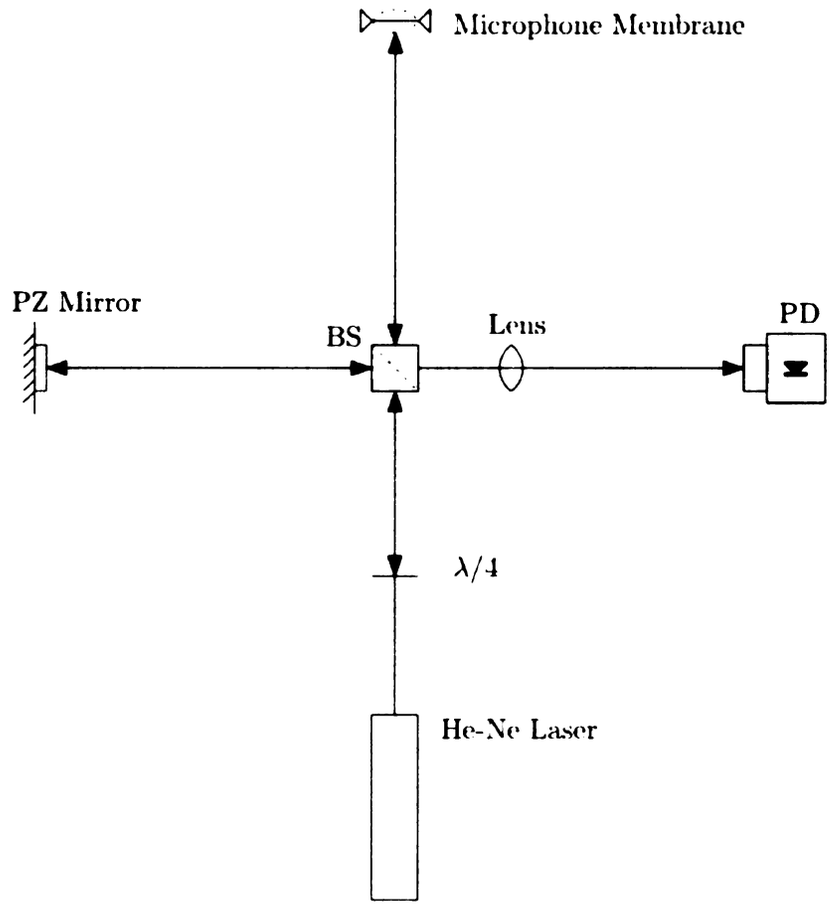

Figure 3.3: Depiction of the optical setup for the Michelson interferometer.

The interferometer's photodetector outputs current in proportion to the incident optical power. Thus, in order to digitally record this output, it must first be converted to voltage. This is accomplished using the "Gain Stage" circuit is shown in Figure 3.6. The photodetector is connected to an input inverting-amplifier through resistor R_1. The frequency bandwidth of the optical sensor is determined from the value of R_1

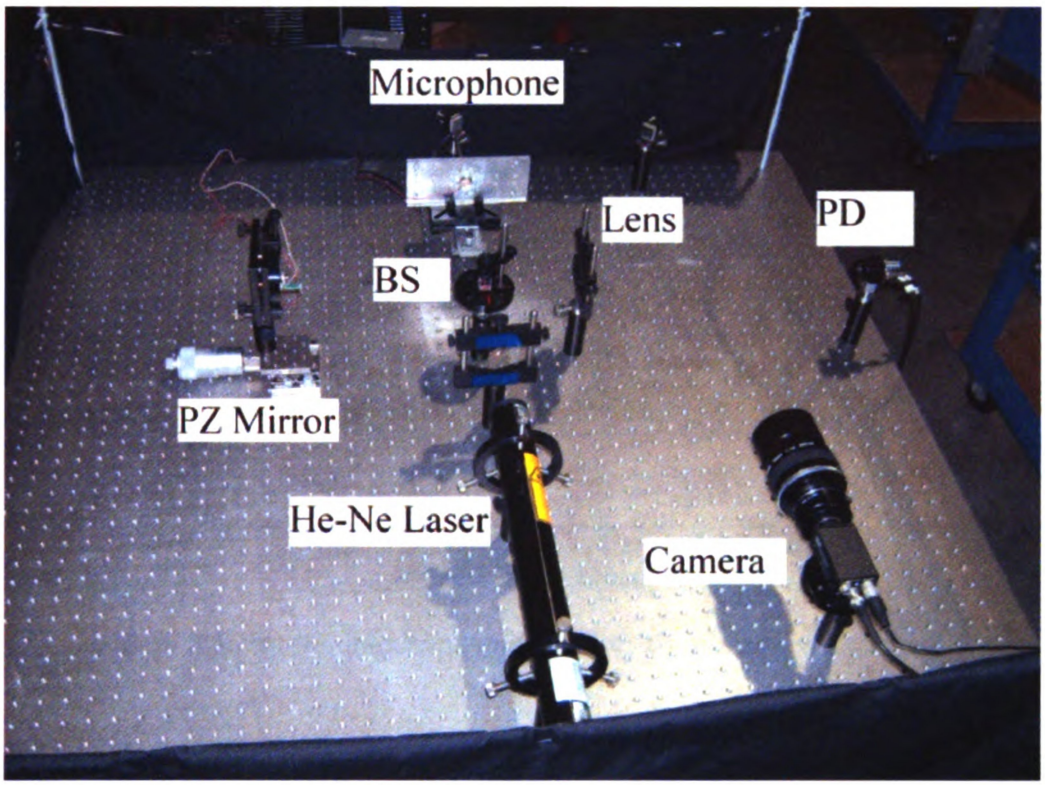

Figure 3.4: Photograph of the optical setup for the Michelson interferometer (Note the placement of a CCD camera and mirrors which aid in alignment of the laser beam with the center of the microphone membrane).

and the diode capacitance C_{PD} of the photodetector (specifically, the time constant of the photodetector is given by $\tau_{PD} = R_1 C_{PD}$). The output voltage of the inverting amplifier is determined by the current output of the photodetector and the value of the feedback resistor R_2 (i.e. $V_{PD} = -I_{PD} R_2$). The second op-amp (operational amplifier) in the circuit is a unity gain inverting amplifier, the output of which is AC coupled with a low frequency cutoff defined by C_1 and R_5. The voltage v_1 is the microphone output signal and is also the signal fed to the phase-lead compensator. The sensitivity of the interferometer used for the results reported in this chapter was 39 mV/nm at the operating set point (see Figure 3.5) for definition of the operating point).

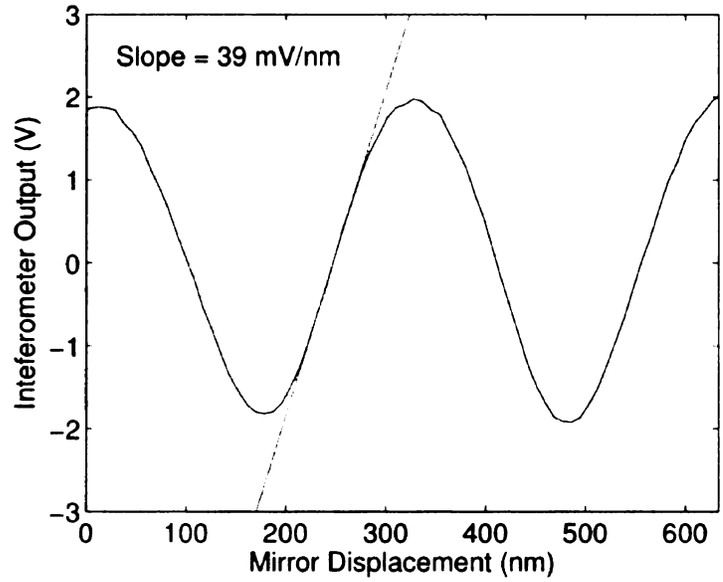

Figure 3.5: Inteferometer output relative to mirror displacement.

An observation made during the initial setup of the Michelson interferometer is that there was prominent low frequency (sub 1Hz) drift that results in the interferometer output signal not maintaining its desired DC set-point and linear operating range. To compensate for this drift, a feedback section is included in the interferometer circuit (see Figure 3.6). At the input op-amp of this feedback section, the voltage output from the gain stage is compared to a fixed voltage set by the potentiometer P_{set}. The feedback gain is set by the resistance of the trim-pot R_G. This output is then fed to a summation amplifier where a DC bias voltage is added with a value defined by $V_{DC} = 12 \cdot R_8/R_{DC}$. The output is then low-pass filtered using a R-C passive filter with a cutoff of approximately 1HZ at v_2 and fed to a ThorLabs model MDT691 piezo amplifier. This amplified output is supplied to the piezo mirror in the reference arm of the interferometer, thus maintaining the output of the interferometer at a constant DC set-point in the sub-1Hz frequency band. A point of note is that a similar system may be used to extend the interferometer's linear range, however, this would require a piezo stack with a resonant frequency that is much greater than the microphone

prototype currently used.

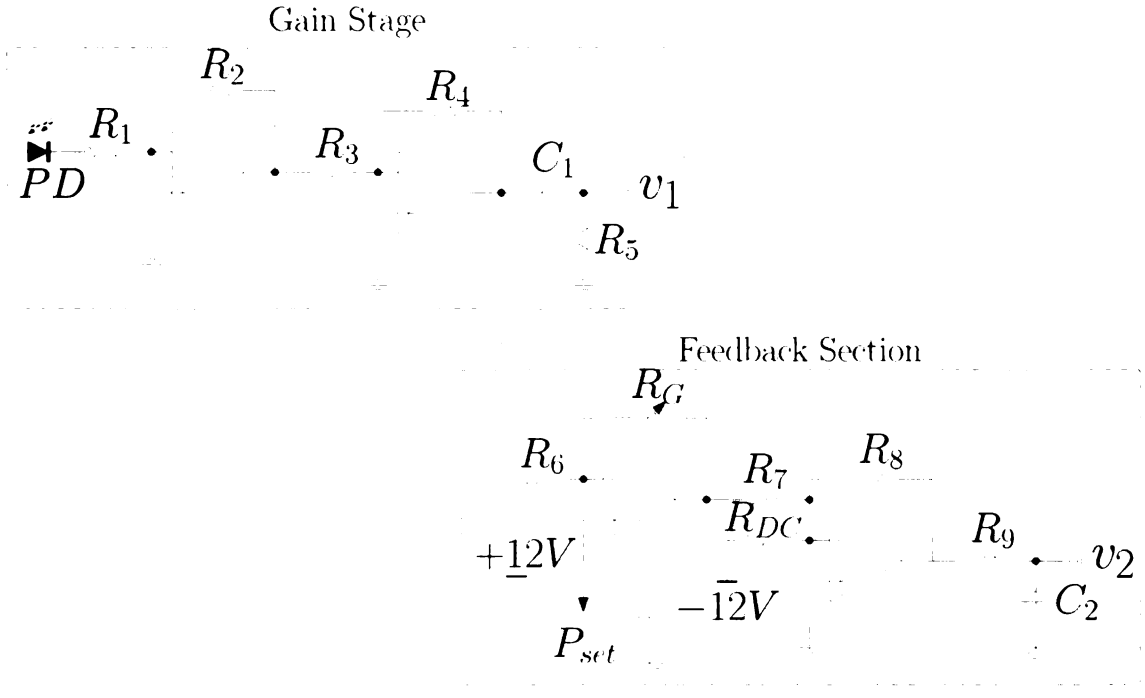

Figure 3.6: Schematic diagram of interferometer circuit, with feedback section.

3.1.3 Serial Interfaced Controller

In addition to the use of a new optical sensor, the design of the compensator circuit was modified to improve the system's operation for the purpose of scalability to beamforming array applications. These modifications allow for all of the phase-lead compensator parameters to be adjusted using a serial interface, which in this case is implemented using the digital output of a National Instruments PCI-6024E general purpose data acquisition (DAQ) board. The added provision allowing to set the parameters of the controller via a computer, when coupled with the open-loop system identification/closed-loop modeling demonstrated in Chapter 2 can be used to fully automate the process of tuning the response of microphones in a large array to a desired ("self-matched") response.

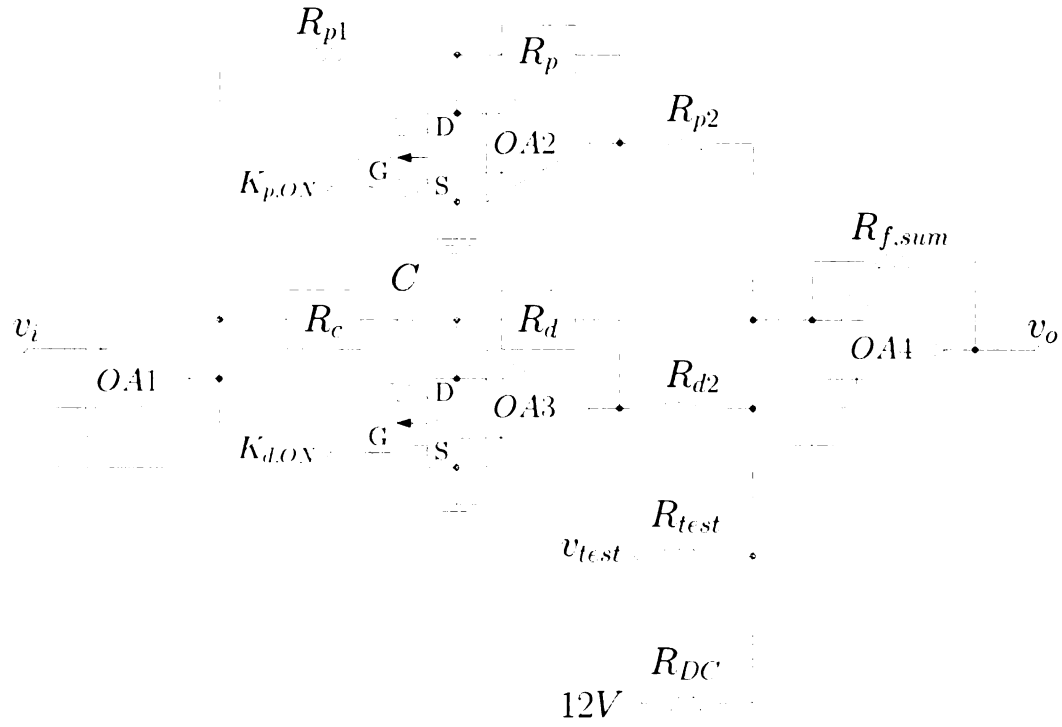

Figure 3.7: Schematic diagram of phase-lead controller circuit.

A schematic of the re-designed compensator circuit is shown in Figure 3.7. The first design modification of the circuit is the replacement of the precision trim-pots used previously with 3-wire serial potentiometers of the MCP42XXX variety manufactured by MicroChip Technologies[2]. These are packaged as 14-pin DIP integrated circuits with two on-chip potentiometers. Each of these potentiometers has 256 incremental resistance values. In the compensator circuit, the two on-board potentiometers are connected in parallel, resulting in a total of 2^{16} possible resistance values. In the microphone control application the available resistance values are placed in order, and a value is chosen based on a calculation of minimum error from the user's input specifications. The three potentiometers, represented by R_p, R_d, and R_c are wired in a daisy chain configuration, as depicted in Figure 3.8. This configuration allows for the resistance values of a large number of serial potentiometer chips to be controlled

[2]`http://ww1.microchip.com/downloads/en/DeviceDoc/11195c.pdf`

by only 3 wires. For each chip, a 16 bit serial signal is sent from the DAQ board, where the first 8 bits determines which potentiometer will be controlled, while the second 8 bits determines the incremental resistance. The chips MCP42050, MCP42100, and MCP42010 correspond to potentiometers with maximum resistance values of 50kΩ, 100kΩ and 10kΩ which have been chosen because they allow for the controller to produce the necessary proportional gain, derivative gain, and time constant used in control of the microphone.

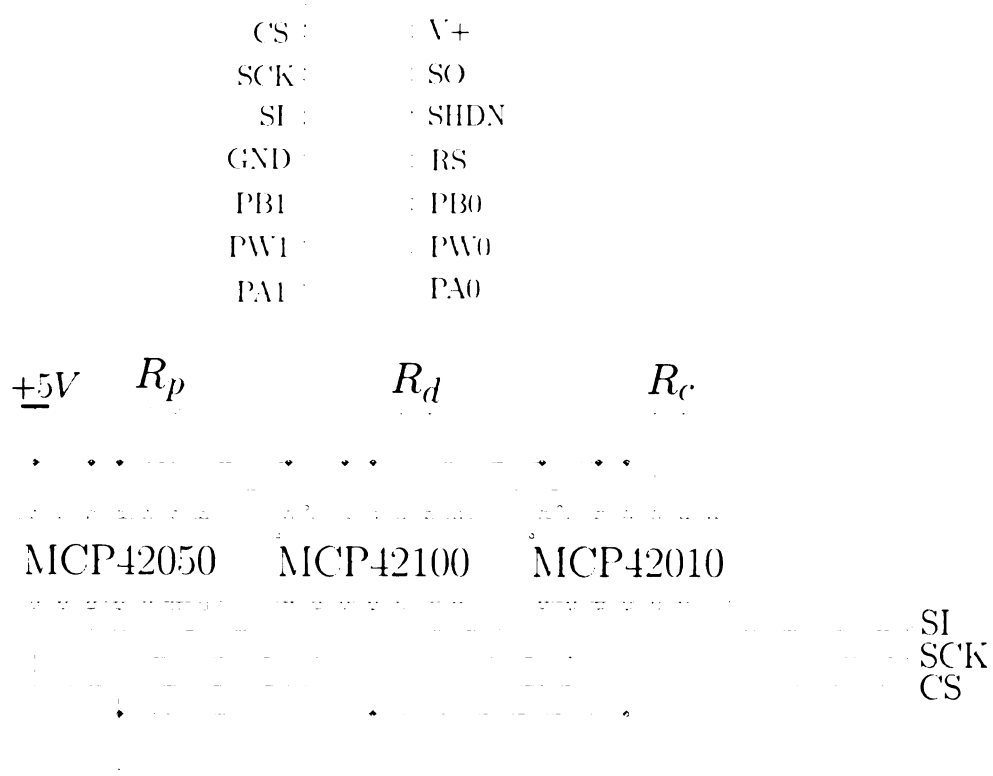

Figure 3.8: Schematic diagram of serial potentiometer interface.

The second design modification is the addition of a N-channel MOSFET switching interface, allowing for fast switching between open- and closed-loop operation. This is done using two separate MOSFETs, one each for the proportional gain and derivative gain sections of the circuit. The drain is connected to the negative input of the op-amp while the source connects to ground. Switching of the proportional and derivative

gain sections is controlled by digital connections at $K_{p,ON}$ and $K_{d,ON}$ respectively. When both MOSFETS are switched on, the input to the gain and derivative sections is forced to zero and hence, no feedback signal is generated resulting in open-loop operation. On the other hand, when one or none of the MOSFETS is turned on, proportional only, derivative only (up to a user-set cut-off frequency), or phase-lead feedback control is implemented. Finally, the circuit has a separate input, v_{test}, for function generator signals used in electrical actuation of the PVDF membrane.

3.2 Experimental Procedure

The experimental procedure used is largely identical to that used in Chapter 2, with various modifications that arise from prototype and compensator design modifications. Similar to the previous work, electrical actuation is used to determine the transfer function of the membrane across a wide frequency bandwidth. Acoustic calibration is used to verify that the frequency response due to acoustic excitation matches that determined through electrical actuation.

In tests performed where the microphone membrane is electrically actuated, there are two notable changes in experimental procedure. The first, as mentioned previously, is the addition of the v_{test} input to the controller circuit. Previously, the output of the function generator was connected directly to the input of the piezo driver. In this new modification, the function generator connects to a unity gain inverting amplifier at the output of the controller. With this and the other previously described modifications to the control circuit, the microphone can be calibrated in either open- or closed-loop operation without replacing any cable connections. This is expected to provide convenience in a large array application where efficiency in the calibration

process is essential.

Second, there were two considerations that had to be taken into account when the system was operated with the Michelson interferometer, requiring modification to the calibration process: (1) at resonance the electrical actuation response can easily become non-linear due to the small linear range of the Michelson interferometer (approximately 79nm compared to 28μm for the fiber-optic lever sensor) requiring the function generator output to be set to a low voltage amplitude, and (2) when operating at this low voltage amplitude, the signal-to-noise ratio at low frequency is greatly sacrificed due to much lower sensitivity in this frequency region.

A convenient method was developed that allows for accurate calibration of the membrane's response despite the trade-off between linearity at resonance at signal-to-noise ratio at low frequency. This method exploits the fact that for a long duration harmonic sweep (i.e. 30s) over a wide frequency band (typically extending from 10Hz to 50kHz), the frequency spectrum of the actuation signal for any single record with short duration (i.e. 30ms) will be dominated by a small number of frequency bins located in the vicinity of the function generator frequency. Thus, a modified calibration program was developed using LabView where after a sensitivity spectrum is acquired for a single record, only the seven entries nearest the peak in the generator signal are appended to an output matrix. Once the program reaches its completion, this output matrix is sorted by frequency, and entries at identical frequency bins are averaged and output to a text file. This method is somewhat analogous to tests where measurements are done at a single fixed frequency, one at a time, while avoiding the inconvenience and lengthy duration of such tests. The method also proves highly effective at maintaining a high signal-to-noise ratio at low excitation amplitudes.

3.3 Results and Discussion

3.3.1 Electrical Actuation

Electrical actuation was performed on the new membrane using the methodology described above, with the results for electrical sensitivity shown in Figure 3.9. Using the new v_{test} input in the controller (see Figure 3.7), the response was tested in both open- and closed-loop operation.

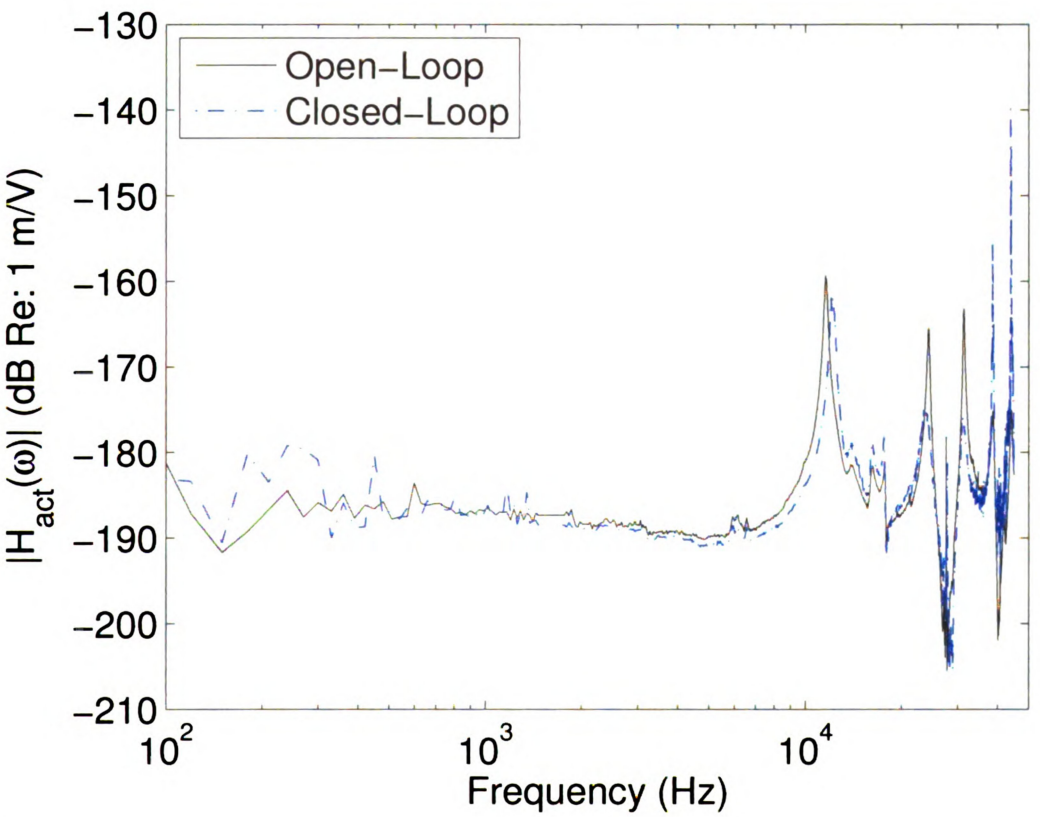

Figure 3.9: Frequency response of 6.35mm membrane with Michelson interferometer, measured using electrical actuation.

The fundamental resonant frequency of the membrane under test was determined from electrical actuation to be 11.6kHz. It can be seen that the response of the fundamental

mode has the characteristics seen previously with the earlier prototype in Chapter 2. However, the higher order resonant peaks are of much greater magnitude than those seen previously for the 12.7mm prototype (see Figure 2.7), and are in some cases at frequencies inconsistent with those predicted for axi-symmetric modes. This renders the system identification methodology described by Equations (2.4)-(2.8) ineffective for the higher order modes. A possible explanation for this behavior is that the forces induced by electrical actuation of the membrane are concentrated at its edges due to the clamping method holding the membrane essentially flat. In contrast, the prototype tested in Chapter 2 had curvature induced by internal pressurization and this would cause electrically induced forces to be near uniformly distributed across the entire surface of the membrane.

More important to this research is the effect that these large magnitude high order resonant peaks have on controllability. In this experiment, the gain settings on the controller were increased until the system was near its stability limit. In the results, there is negligible DC attenuation resulting from the feedback control, while the resonant frequency has been increased to 12.2kHz in closed-loop operation, a 5% increase. A magnified plot depicting the change in resonant frequency in closed-loop operation can be seen in Figure 3.10. This is clearly insufficient for the current prototype to satisfy the demand for a "self-matching" microphone array. Still, with certain design modifications (see Chapter 4) the smaller diameter prototypes hold promise.

3.3.2 Acoustic Calibration

Acoustic calibration was performed in addition to electrical actuation to verify the effectiveness of the latter as a calibration method. A plot of sensitivity measured up

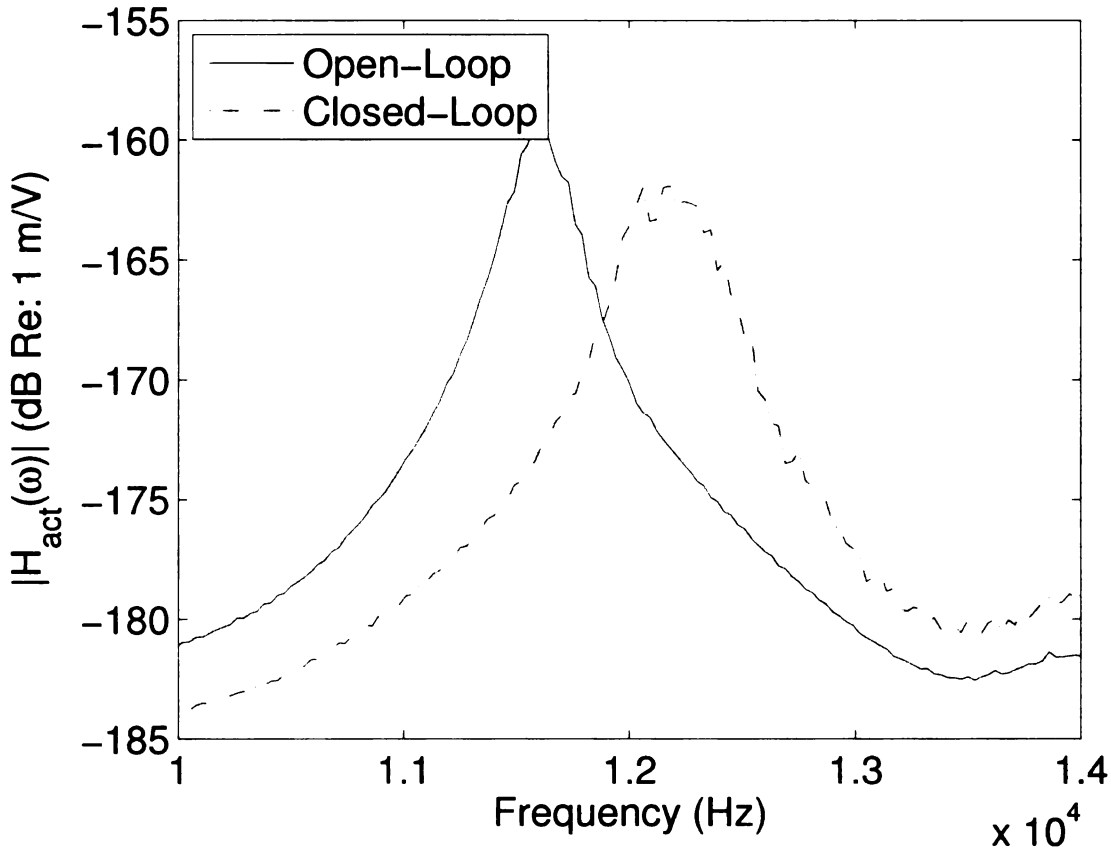

Figure 3.10: Frequency response of 6.35mm membrane with Michelson interferometer, measured using electrical actuation, magnified to show frequencies near the fundamental resonance.

to the plane wave tube cutoff frequency of 21kHz is shown in Figure 3.11. The low frequency sensitivity of the microphone was measured at 3kHz and determined to be 177 mV/Pa. It can be seen in the plot that below 2kHz the calibration does not adhere to the flat profile expected. It is possible that this results from the acrylic channel that forms the plane wave tube being significantly shorter (15 cm) than the one used previously, resulting in an unpredictable acoustic field at low frequency. However, the frequencies of interest are near the fundamental resonant peak, where it can be observed that the behavior is much the same as that of the electrical actuation.

A second test was performed to characterize the sensor's linearity. Based on the

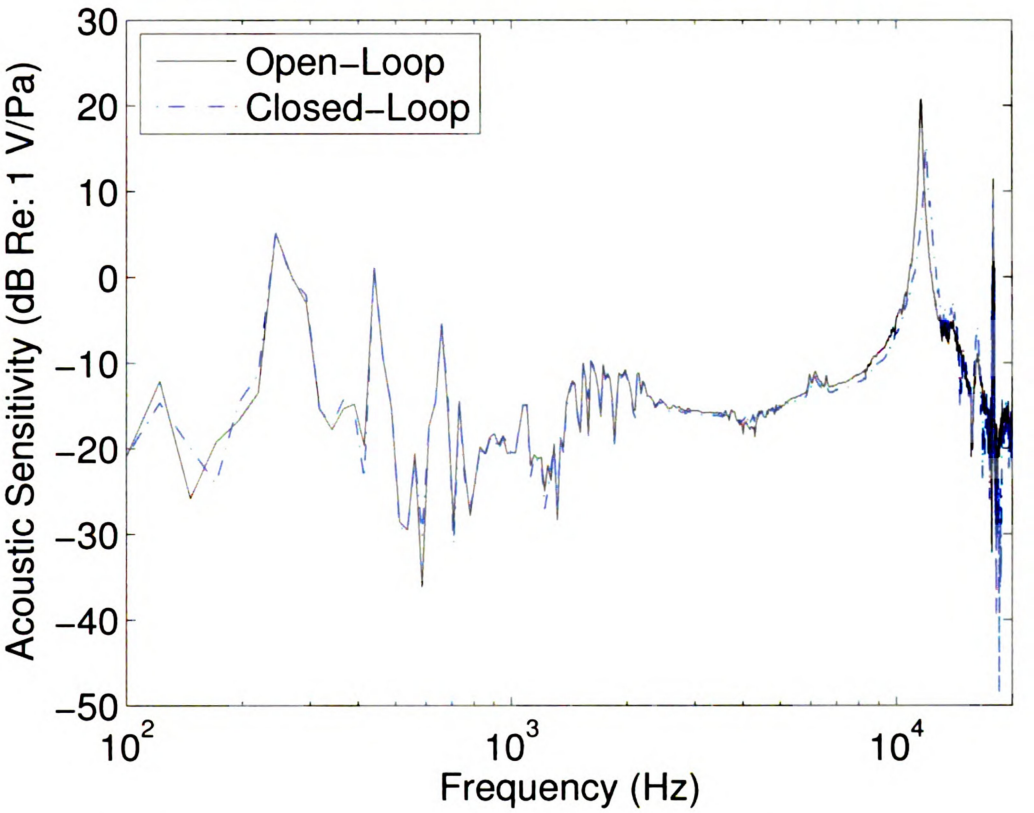

Figure 3.11: Frequency response of 6.35mm membrane with Michelson interferometer, measured using acoustic calibration in a plane wave tube.

operating principle of the interferometer, the output voltage is expected to vary sinusoidally with a period equal to half the optical wavelength with respect to target deflection. The feedback circuit described previously is designed to force the DC setpoint of the interferometer to the highest sensitivity operating region. When the membrane's vibrational amplitude becomes very large the voltage output begins to distort in a manner similar to saturation.

To demonstrate the effects of linearity and determine the dynamic range of the sensor, acoustic testing was performed in the plane wave tube setup with the prototype microphone operating in open-loop mode. A harmonic tone was supplied by the function generator to an amplifier and speaker. For each data point an average of

16 spectra was obtained using a sample rate of 50kHz and bin width of 1Hz. Data were acquired with acoustic tones generated at 3kHz as well as 12kHz in order to differentiate the performance of the sensor in the low frequency "flat" region of its response from its performance near resonance. The results are reported in Figure 3.12, where rms voltage of the prototype sensor is plotted versus the sound pressure level (SPL) measured by the reference microphone. A linear trend-line has been fit to the data, corresponding to sensitivity at that frequency. The sensitivities calculated from the slope of these trend-lines were 177mV/Pa at 3kHz and 1930mV/Pa at 12kHz, significantly higher than the sensitivity of the previous prototype using the fiber-optic lever sensor. Deviations from the trend-line at high sound pressure levels indicate the onset of non-linearity.

It can be observed from Figure 3.12 that for a 3kHz tone the data points begin to deviate from the linear fit as SPL approaches 110dB (6.3 Pa). The measured values at low SPL for the prototype microphone closely track the linear fit, indicating that the noise floor for the microphone is very low, perhaps comparable to, or better than that of the B&K reference microphone. For the 12kHz tone the non-linearity associated with the Michelson interferometer becomes more clearly apparent at lower SPL. The output of the prototype begins to deviate from the linear fit at approximately 90dB (0.63 Pa), before dropping sharply. It was observed at this point that odd-numbered harmonic overtones begin to dominate the signal. This becomes a matter of practical importance when performing "white noise" acoustic calibration where it is important to operate the speaker at a high enough level to maximize signal-to-noise without distortion. The smaller linear range of the Michelson interferometer is an important distinction to be made in comparison to the fiber-optic lever sensor. However, it is important to note that this non-linearity is for the open-loop operation. In closed-loop operation with strong control authority, the sensor's linearity should be enhanced

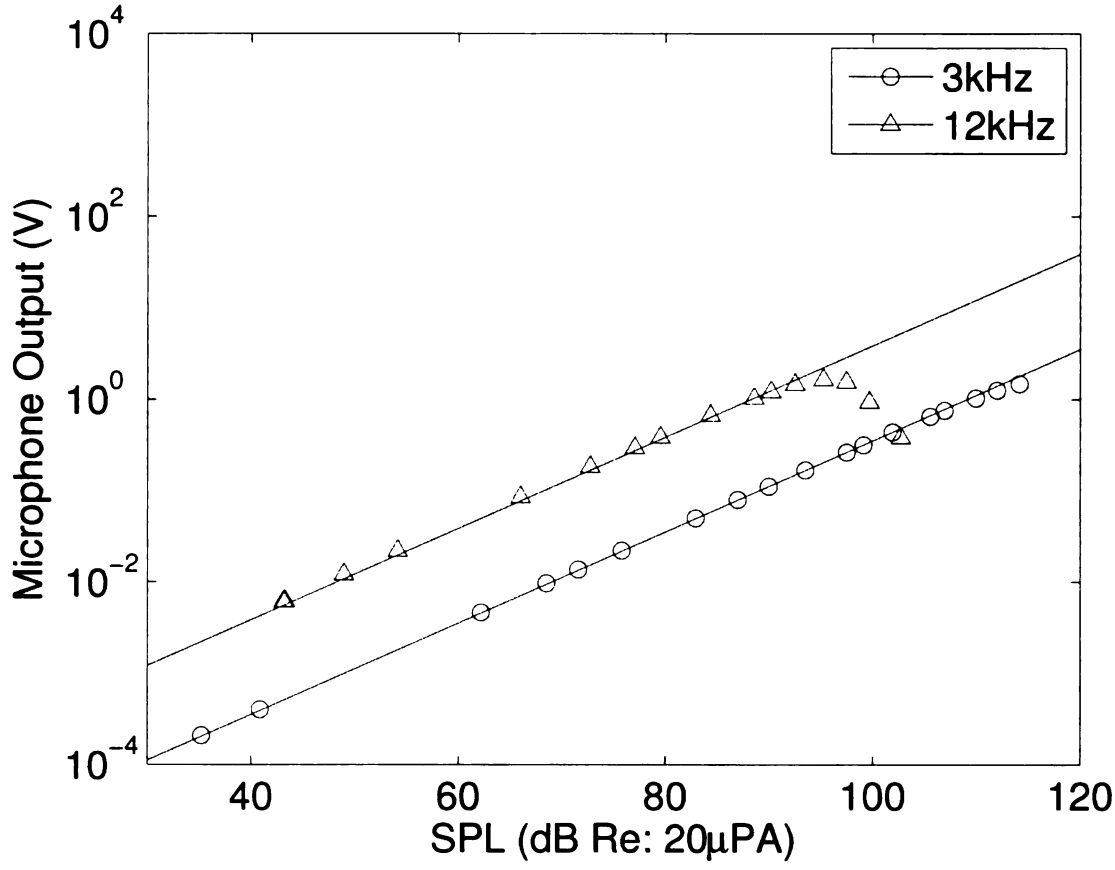

Figure 3.12: Linearity of 6.35mm membrane with Michelson interferometer, measured using acoustic calibration in plane wave tube at 3kHz and 12kHz.

substantially.

3.3.3 Comparison of Michelson Interferometer to Fiber-Optic Lever Sensor

In comparing the performance of the Michelson interferometer to the fiber-optic lever displacement sensor, important trade-offs must be made in regards to sensitivity, resolution, linear range, and frequency bandwidth. Values for these parameters for both sensors are given in Table 3.1, where the sensitivity of the fiber-optic lever sensor and all parameters for the Michelson interferometer are experimentally calibrated, while

resolution, linear range, and frequency bandwidth of the fiber-optic lever sensor are taken from its user manual. The reported bandwidth of the Michelson interferometer is calculated from the photodetector capacitance and input resistance of the circuit (i.e. Bandwidth = $1/(2\pi R_1 C_{PD})$, while the dynamic range of the interferometer is calculated as $\lambda/8$ where λ =633nm.

Table 3.1: Comparison of sensor parameters between fiber-optic lever and Michelson interferometer.

Sensor Type	Sensitivity	Resolution	Linear Range	Bandwidth
Fiber-Optic Lever	86mV/μm	0.025 μm	23μm	20kHz
Michelson Interferometer	39mV/nm	NR	79nm	8MHz

The clearest advantage for using the Michelson interferometer over the commercial fiber-optic lever is the significant increase in sensitivity. The Michelson interferometer and associated circuitry have shown an increase in sensitivity by a factor of about 450 over the fiber-optic lever sensor. The noise floor is also expected to be a significantly lower, though this is not reported at this time due to the difficulties in achieving a "silent" experimental setup. The trade-off to the increased sensitivity of the Michelson interferometer is its much smaller dynamic range.

Another comment to be made when comparing the two sensors is regarding simplicity of use. The fiber-optic lever is very simple to operate as it requires only a fixture and traverse table for aiming it at a target. More permanent designs can be envisioned where the fiber probe is threaded and attached directly to the microphone capsule. The current design of the Michelson interferometer requires careful alignment when setting up, and requires additional electrical circuitry for operation. However, alignment problems could be overcome if future sensors were packaged using fiber-optics.

Chapter 4

Theoretical and Experimental Evaluation of Proposed Design Improvements

In Chapters 2 and 3 it was observed from calibration data that several high-order membrane resonance modes are excited during electrical actuation. These modes have been determined to be a primary cause of instability that occurs in closed-loop operation. While the data presented indicates the current design is practical for "self-calibration" and "self-matching" of microphones in an array application, it leaves room for improvement in terms of controllability. For this purpose, two basic modifications are suggested. (1) development of an optical sensor that averages displacement over a large fraction of the area of the microphone membrane, and (2) modification of the mechanical parameters of the microphone capsule, specifically adding a perforated back-plate to increase damping. Justification for these two methods are given in the sections below.

4.1 Displacement Averaging Optical Sensor

As noted previously, the microphone's open-loop dynamics can be modeled using the linear wave equation for a stretched thin membrane. The wave equation gives rise to an infinite number of axisymmetric and non-axisummetric modes of membrane vibration. For the case where the optical sensor measures displacement of a point at the center of the membrane, it was determined that the membrane could be modeled as a summation of second order systems, with each system representing the transfer function for the corresponding axi-symmetric mode. Non-axisymmetric modes are neglected, as they have zero magnitude at $r = 0$. A drawback of this method is that the axi-symmetric modes are prominent in the center measurement and result in instability during closed-loop operation.

The proposed alternative is to incorporate an optical sensor that measures the average displacement of the membrane over a large portion of its area. It is shown in [22] that the axi-symmetric modes of a circular membrane clamped at its edges take the shape of Bessel functions of the zeroth order. A plot depicting these mode shapes for the fundamental resonant mode, in addition to the first through third modes is shown in Figure 4.1. The shapes of the higher order resonant modes are notable for the fact that there are regions on the membrane that are 180° out of phase with the center of the membrane. The result is that the displacement for these modes averaged over the surface of the membrane is significantly smaller than the displacement measured at the center.

Mathematical analysis can be employed to prove the attenuation of these higher order modes by use of a displacement averaging sensor. The average displacement relative to z_c, z_{avg}/z_c, over the area of the membrane for the m^{th} mode can be

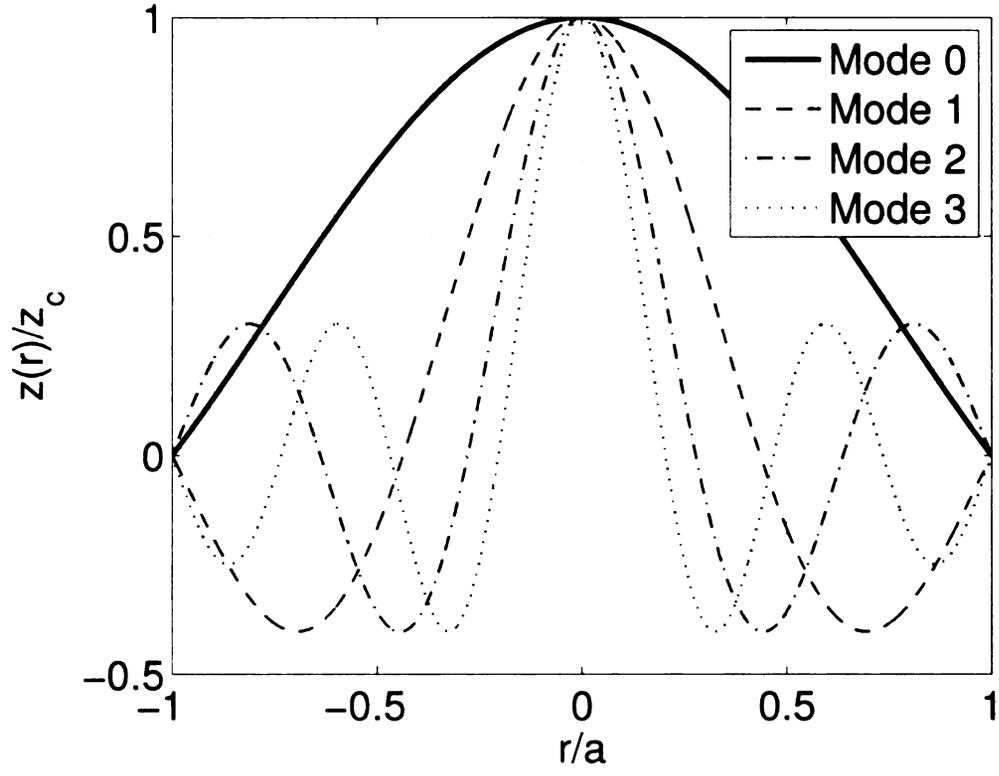

Figure 4.1: Axi-symmetric mode shapes of a vibrating membrane.

calculated by equation (4.1), where a_s/a is the optical sensor radius as a fraction of the membrane radius, J_0 is the bessel function of the zeroth order, k_m is the wavenumber associated with the m^{th} mode, and r and θ are polar coordinates in the plane of the membrane.

$$\frac{z_{avg}}{z_c} = \frac{1}{\pi(a_s/a)^2} \int_0^{2\pi} \int_0^{a_s/a} J_0(k_m r) r dr d\theta \tag{4.1}$$

By solving equation (4.1) with $a_s/a = 1$ the average relative displacement magnitudes of the corresponding modes over the *entire* membrane surface is known. The magnitude of this displacement for several of the modes is listed in Table 4.1 and is plotted in Figure 4.2.

Table 4.1: Average relative displacement of membrane vibrational modes over the entire surface of the membrane.

Mode	z_{avg}/z_c
0	0.4314
1	-0.1234
2	0.0627
3	-0.0394
4	0.0277
5	-0.0208
6	0.0163
7	-0.0133
8	0.0111

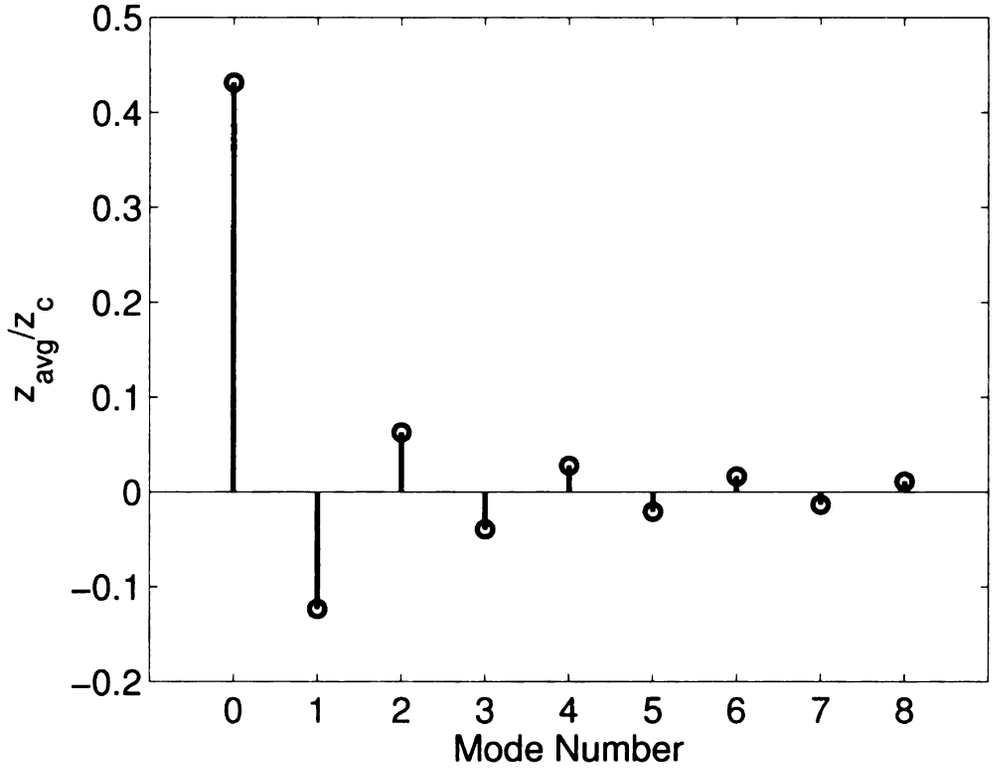

Figure 4.2: Average relative displacement of membrane vibrational modes over the entire surface of the membrane.

Further, this methodology can be extended to design for the optimal probe diameter to maximize attenuation of a particular mode. By selecting a_s such that $0 < a_s/a < 1$, average displacement for optical sensors that are a fraction of the total membrane

radius can be calculated. It can be shown using equation 4.1 that for certain values of the averaging radius (a_s), which are a fraction of the microphone membrane diameter, individual modes can in fact be cancelled completely (for example, at $a_s/a = 0.69$ the average displacement of mode 1 is 0). The magnitudes of the average displacement of modes 0-3 for variation in relative probe diameter are shown in Figure 4.3. Note that as the optical sensor radius approaches the radius of the membrane the averaged displacements converge to the values given in Table 4.1 and Figure 4.2.

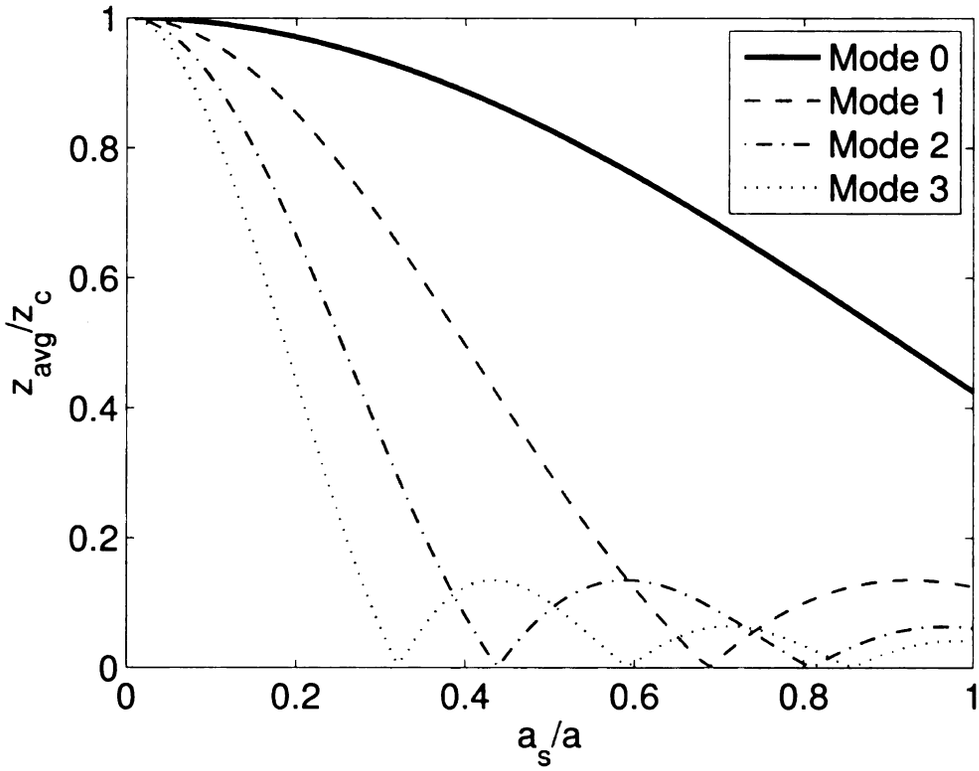

Figure 4.3: Relative average displacement of membrane as a function of the sensor probe diameter.

To demonstrate the value of using a displacement averaging sensor, the magnitudes of average displacement over the area of the optical sensor, illustrated by Figure 4.3, are used to multiiply the second-order transfer function of their respective modes in the membrane's transfer function (see equation (2.8)), in this example using membrane

parameters calculated from the prototype used in Chapter 2. For this study, two different sensor sizes were chosen. First, the ratio of $a_s/a = 0.37$ was chosen, as this corresponds to an optical sensor of 4.76mm diameter (which is available commercially; see end of this section) being used for measurement of the 12.7mm prototype capsule. Second, the ratio of $a_s/a = 0.69$ was chosen, as this appears to be an optimal case due to the anticipated complete cancellation of mode 1. Plots of the theoretical frequency response of the open-loop for these two sensor diameters are shown in Figures 4.4 and 4.5, where the sensitivity has been normalized with respect to the theoretical DC response. Clearly, in both cases controllability would be improved by an increase in gain margin resulting from the reduction in magnitude of higher modes, especially in the optimal case where $a_s/a = 0.69$. Also, the phase behavior of the sensor with $a_s/a = 0.69$ should be noted as it appears to asymptote to 180° at high frequency, compared with the center measurement where there is a 180° phase transition associated with each resonant peak.

As an example of sensors currently available commercially that measure average displacement over an area larger than the fiber-optic lever currently in use, the reader is reffered to models manufactured by Philtec[1]. In particular, the Model D169 has a probe diameter of 4.76mm with a sensitivity of $40mV/\mu m$ and 100Hz resolution of $0.008\mu m$. The performance of this sensor is comparable to the Model D20 employed here, while having the desired larger diameter.

[1] http://www.philtec.com/09GuideJuly_13.pdf

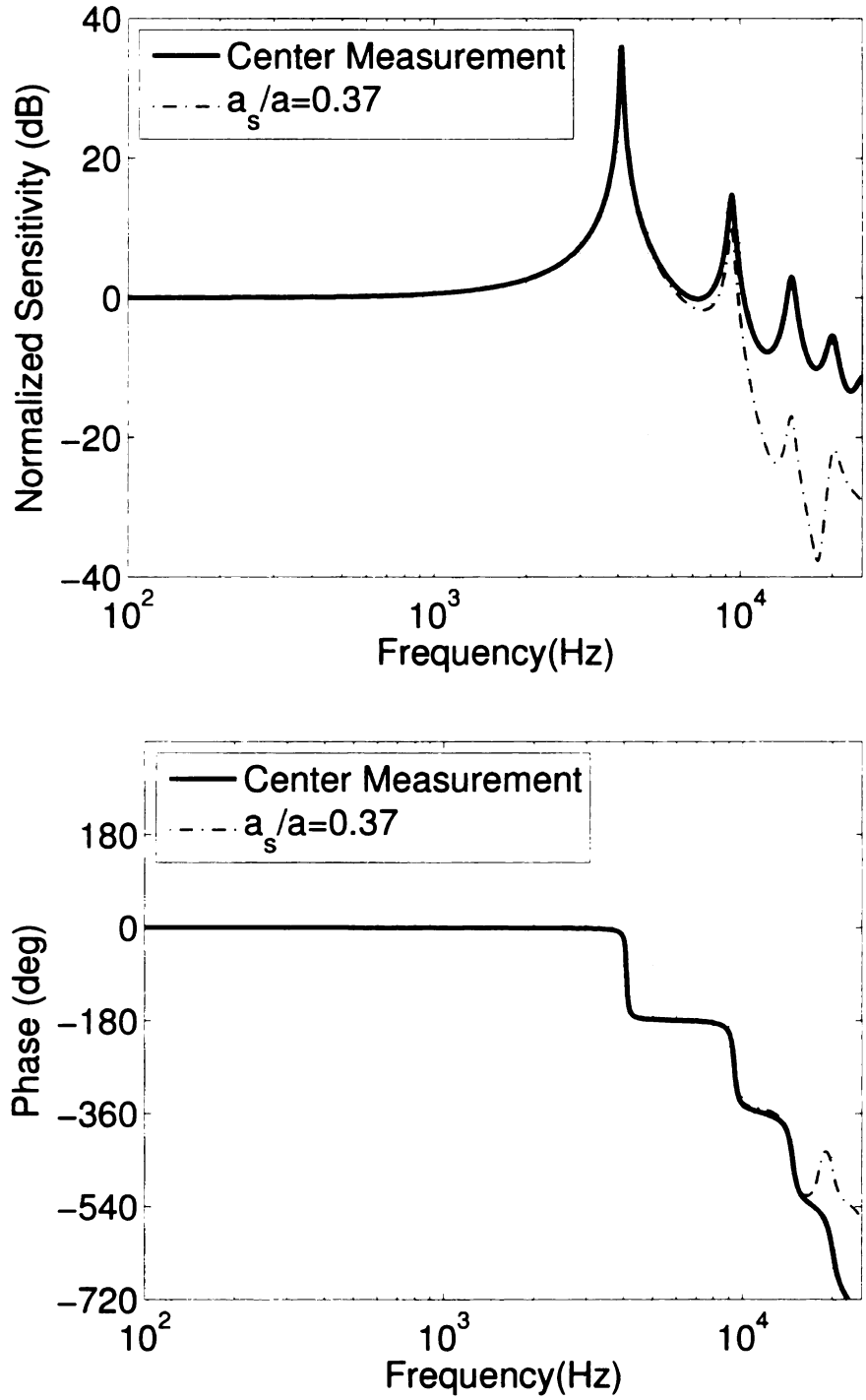

Figure 4.4: Theoretical frequency response of the open-loop when measuring the membrane deflection at its center (solid line) compared to when using an optical sensor with a_s/a =0.37

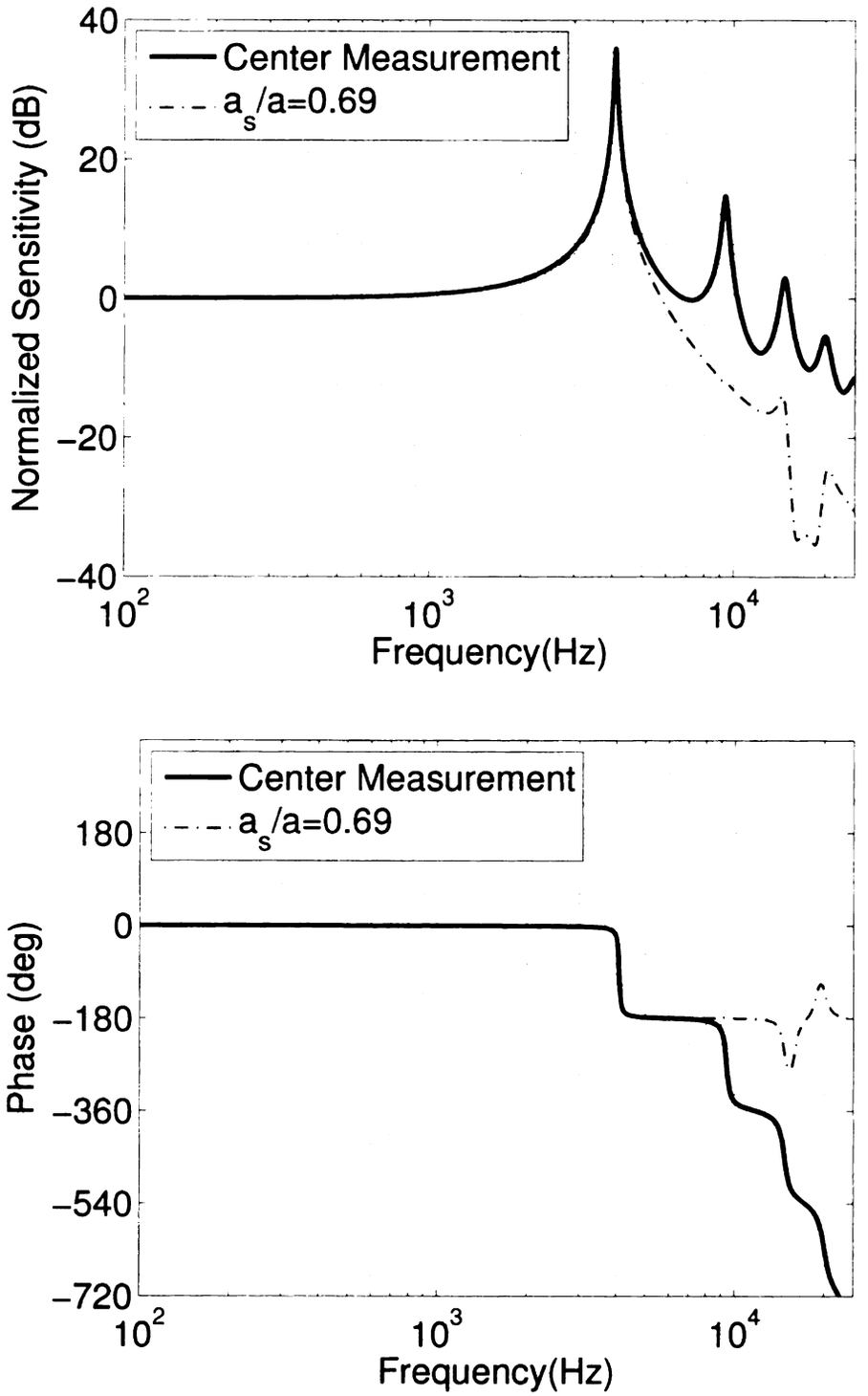

Figure 4.5: Theoretical frequency response of the open-loop when measuring the membrane deflection at its center (solid line) compared to when using an optical sensor with a_s/a =0.69

4.2 Perforated Back-Plate

As seen from calibration results, the microphone prototype tested had very low damping (ζ=0.006 for the fundamental mode) resulting in very sharp peaks for each of the resonant modes. An increase in available gain margin and general improvements in controllability are expected if a mechanical damping provision is added to future prototype capsules. This would be achieved using a perforated back-plate, similar to what is common in commercial condenser microphones.

A method for analytical design of a perforated back-plate is discussed in [25]. Equations (4.3)-(4.6), which are taken from this reference, describe the back-chamber pressure which resists the membrane motion. These equations are based on the electrical analogy of the "air mass" oscillation through holes in the back-plate. The equivalent circuit for the analogy is shown in Figure 4.6. In the circuit, each hole is represented by an inductance in series with a resistance. The inductance models the inertia of the air inside the hole, and the resistance represents dissipative effects analagous to damping. The back-chamber behind the back-plate acts as a compliance element, and hence is modeled as an electrical capacitance. Using this electrical circuit model, the pressure drop across hole k can be calculated as follows:

$$p_k = u_k Z_k + \sum_{k=1}^{q} u_k Z_C \tag{4.2}$$

where Z_k is the acoustic impedance of the k^{th} hole, u_k, the acoustic velocity, is equivalent to the electrical current, Z_C is the acoustic impedance of the back-chamber and $\sum_{k=1}^{q} u_k$ is equivalent to the sum of all currents passing through the inductance-resistance branches representing holes in the back-plate. Equation (4.2) can be written

in matrix form to represent the pressure drop for all holes in the back-plate as given by equations (4.3) and (4.4).

$$P_b = Z_b U_b \tag{4.3}$$

$$P_b = \begin{bmatrix} p_1 \\ p_2 \\ \cdot \\ \cdot \\ \cdot \\ p_q \end{bmatrix}, \quad U_b = \begin{bmatrix} u_1 \\ u_2 \\ \cdot \\ \cdot \\ \cdot \\ u_q \end{bmatrix}, \tag{4.4}$$

$$Z_b = \begin{bmatrix} Z_1 + Z_C & Z_C & \cdot & \cdot & Z_C & Z_C \\ Z_C & Z_2 + Z_C & \cdot & \cdot & \cdot & \cdot \\ \cdot & Z_C & & & \cdot & \cdot \\ \cdot & & & & \cdot & \cdot \\ \cdot & \cdot & & & Z_{q-1} + Z_C & Z_C \\ Z_C & \cdot & \cdot & \cdot & Z_C & Z_q + Z_C \end{bmatrix}$$

The back-chamber impedance can be computed using

$$Z_C = \frac{\gamma \rho_0 c_I^2}{j\omega V_b} \tag{4.5}$$

where γ is the specific heat ratio for air, ρ_0 is air density, c_I is the isothermal speed of sound through air and V_b is the back-chamber volume. The acoustic impedance of

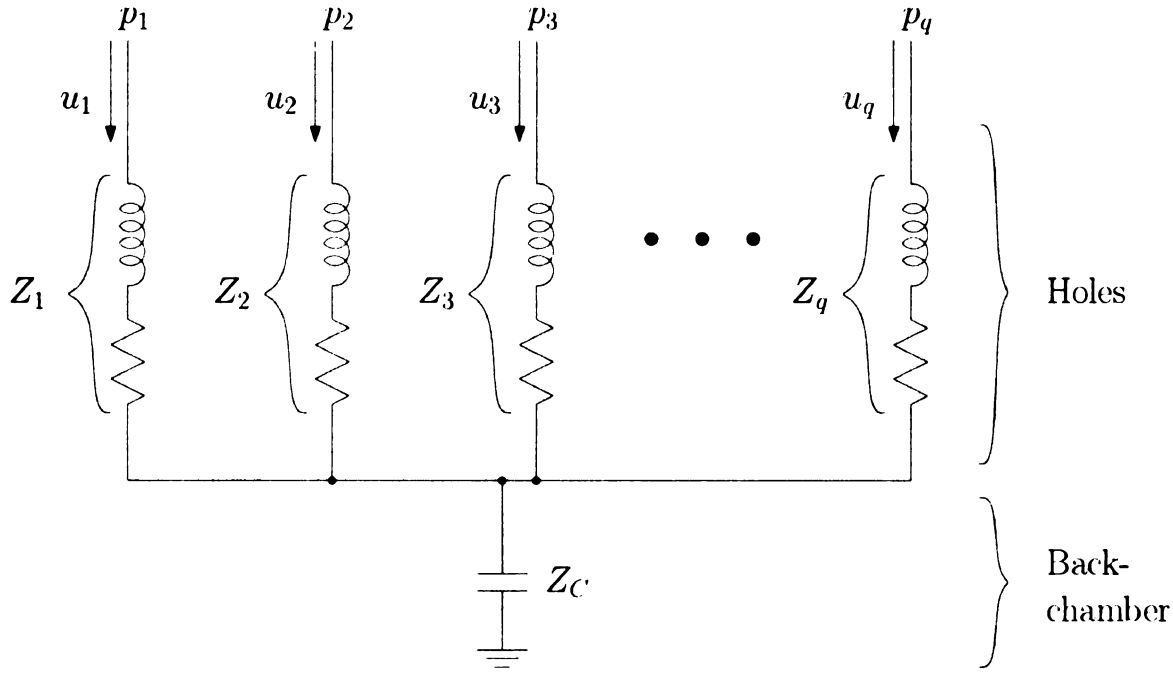

Figure 4.6: Equivalent circuit of the perforated back-plate and back-chamber.

a hole can be calculated using

$$Z_k = \frac{(8\omega\rho_0\mu)^{1/2}}{\pi r_k^2}\left(1 + \frac{l_k}{2r_k}\right) + j\frac{\omega\rho_0(l_k + 1.7r_k)}{\pi r_k^2} \tag{4.6}$$

where μ is air viscosity, r_k is the hole's radius, and l_k is the hole's length.

For purposes of control design, it is desired that Equation (4.3) be such that it can be integrated into the membrane transfer function with ease. Specifically, considering the transfer function of a second-order system, representing the membrane's dynamics through the fundamental resonance, the back-pressure resisting the membrane motion (p_k) can be added as a forcing term:

$$(M_0 s^2 + C_0 s + K_0)Z_c(s) = P(s) - P_k(s) \tag{4.7}$$

where $P(s)$ is the Laplace transform of the acoustic pressure acting on the outside surface of the membrane and P_k is the Laplace transform of the resisting back-pressure. A Simplified transfer function relating $P_k(s)$ to $Z_c(s)$ can be obtained if only "piston-like" displacement of the membrane is considered. Related to this restriction, it is further assumed that the air motion through all holes is identical; i.e. $p_1 = p_2 = \cdots = p_q$ and $u_1 = u_2 = \cdots = u_q$. With these, the current approach departs from the elaborate analysis in [25]. However, the method used in the latter is too complex to enable the easy incorporation of the back-pressure in the membrane's transfer function.

With the above simplifications, equation (4.2) becomes:

$$p_k = (Z_k + qZ_C)u_k \tag{4.8}$$

where q represents the total number of holes. The volume velocity can be computed as the volume displaced by the membrane motion per unit time. For this analysis, only the air displaced by the first harmonic mode will be considered. The total volume of displaced air (V_{disp}) due to the fundamental mode can be calculated from the average membrane displacement multiplied by surface area A. Taking the ratio z_{avg}/z_c for the fundamental mode from Table 4.1, this displaced volume is:

$$V_{disp} = 0.4314 \cdot z_c A \tag{4.9}$$

For harmonic oscillation at angular frequency ω, the amplitude of this volume velocity through a single hole is given by:

$$u_k = \frac{0.4314 \cdot z_c A}{q} j\omega \tag{4.10}$$

Substituting from equation (4.10) along with equations (4.5) and (4.6) into equation (4.8) yields an equation for the resisting pressure as a function of center displacement z_c and frequency ω. After being transformed into the Laplace domain (i.e. letting $j\omega = s$), this equation becomes

$$P_k(s) = 0.4314 \cdot Z_c(s) A \left[\frac{\rho_0 (l_k + 1.7 r_k)}{q \pi r_k^2} s^2 \quad + \right. \\ \left. \frac{(8 \omega \rho_0 \mu)^{1/2}}{q \pi r_k^2} \left(1 + \frac{l_k}{2 r_k} \right) s \quad + \quad \frac{\gamma \rho_0 c^2}{V_b} \right] \tag{4.11}$$

Substituting equation (4.11) in (4.7), it can be seen that the influence of the resisting pressure on the membrane dynamics can be modeled as an added inertial mass, damping and stiffness terms that are related to the air layer in the capsule back-plate and back-chamber. These can be represented by equations (4.12)-(4.14). In equation (4.13), the $\omega^{1/2}$ term that exists in the numerator has been replaced with the square root of the fundamental resonant frequency $\omega_0^{1/2}$. This has been shown to be a reasonable approximation as the damping term is dominant only near this frequency. This substitution linearizes the air layer damping term so that its transfer function may be easily used in control system modelling.

$$M_{0b} = 0.4314 \cdot A \frac{\rho_0 (l_k + 1.7 r_k)}{q \pi r_k^2} \tag{4.12}$$

$$C_{0b} = 0.4314 \cdot A\frac{(8\omega_0\rho_0\mu)^{1/2}}{q\pi r_k^2}\left(1 + \frac{l_k}{2r_k}\right) \tag{4.13}$$

$$K_{0b} = 0.4314 \cdot A\frac{\gamma\rho_0 c_T^2}{V_b} \tag{4.14}$$

These terms can be added into the membrane transfer function given in Equation (4.7) yielding

$$H(s) = \frac{1}{(M + M_{0b})s^2 + (C_0 + C_{0b})s + K_0 + K_{0b}} \tag{4.15}$$

To demonstrate the effectiveness of the analytical model in predicting the additional damping provided by a perforated back-plate, capsule inserts were machined and tested. These inserts were machined from acrylic rod stock and designed to fit inside the sealed back-chamber of the 12.7mm prototype capsule described in Chapter 2 (see Figure 2.1). Holes were drilled in the face of these inserts to emulate perforations, where their length and the back-chamber volume is known from measured dimensions. A depiction of one of these inserts and the modified capsule prototype is shown in Figure 4.7.

A total of five of these inserts were constructed and tested. A list of parameters for each of the inserts is given in Table 4.2. In addition, calculated terms for inertial mass, damping and stiffness added by the air layer are given in Table 4.3. Hole length and back-chamber volume are measured using Vernier calipers, while hole radius is based on the size of the drill bit used. It should be noted that there is expected uncertainty in this dimension due to vibration while drilling and thermal interactions with the acrylic material (i.e. expansion/contraction). Also, dimensions

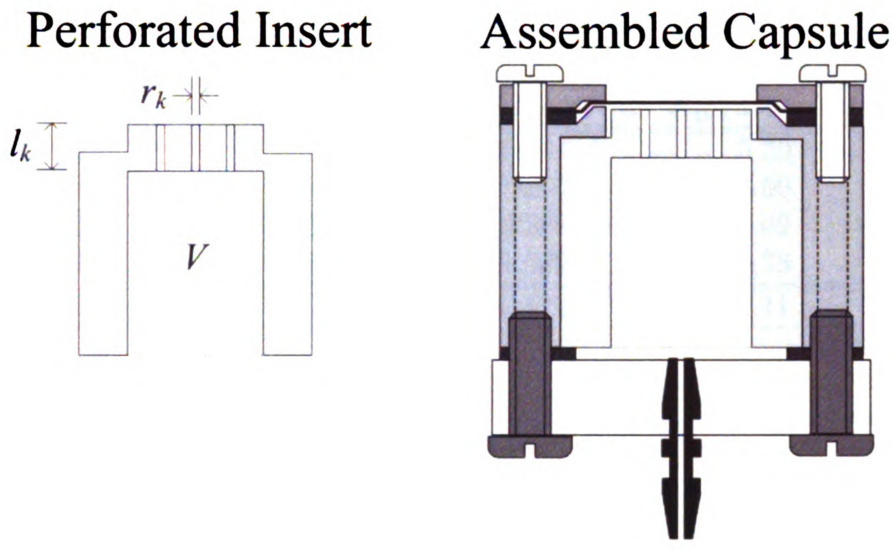

Figure 4.7: Schematic drawing of prototype microphone capsule with acrylic insert designed to simulate a perforated back-plate.

are not considered "ideal" as they are limited by the geometric scales available in a conventional machining process, as better performance is possible with smaller radius holes.

Table 4.2: Known or measured parameters of the acrylic inserts used for verification of the mechanical damping model.

Insert	q	r_k(mm)	l_k(mm)	V_b(cm^2)
1	44	0.508	6.22	2.01
2	19	0.508	6.28	1.81
3	6	0.508	6.52	1.78
4	1	0.508	5.65	1.89
5	18	0.254	4.48	2.12

Initial experiments were conducted using inserts 1-4, where back-chamber volume, hole radius, and hole length were kept nearly constant, and the number of holes were varied. Electrical actuation was performed to determine the frequency response of the modified capsule and verify that it conformed to the model. The frequency response associated with each of the inserts along with their predicted response is shown in Figure 4.8.

Table 4.3: Calculated parameters of the acrylic inserts used for verification of the mechanical damping model.

Insert	q	$M_{0b}(kg/m^2)$	$C_{0b}(kPa \cdot s/m)$	$K_{0b}(MPa/m)$
1	44	0.0178	0.0378	5.39
2	19	0.0415	0.0882	5.99
3	6	0.136	0.289	6.09
4	1	0.717	1.529	5.73
5	18	0.121	0.512	5.11

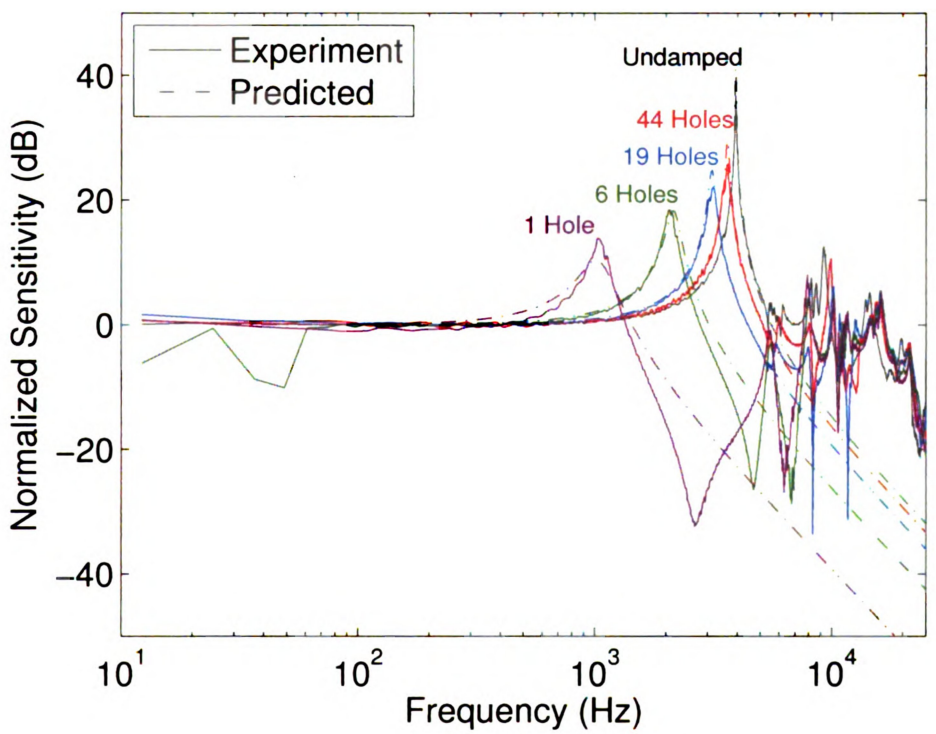

Figure 4.8: Experimental frequency response of microphone membrane with perforated inserts where the number of holes is varied.

The first observation to be made from Figure 4.8 is the relation between the number of holes and the corresponding air layer mass and damping. It can be seen that the desired damping effect increases with fewer holes, as this results in increased fluid velocity through the individual holes. However, inertial mass also increases resulting in an undesirable decrease in natural frequency. A mathematical observation can

be made to show that the ratio of inertial air mass to damping of the air layer has only one variable parameter, r_k. An approximation for this ratio is given in equation (4.16), where it is assumed $(l_k + 1.7r_k) \approx (l_k + 2r_k)$ as it is typical that $r_k \ll l_k$.

$$\frac{M_{0b}}{C_{0b}} = \left(\frac{\rho_0}{2\omega_0\mu}\right)^{1/2} r_k \tag{4.16}$$

Thus, it is inferred that in order to effectively design a perforated back-plate with minimal mass contribution, a very small hole radius, r_k, is ideal. After determining this radius, hole length l_k and the number of holes, q, can be chosen to achieve the desired open-loop damping. With these observations in mind, the improved insert 5 was designed and constructed. Referring to Table 4.3 it can be seen that this insert has a slightly smaller mass contribution than insert 3, while having nearly twice the damping. The frequency response of the improved insert is shown in Figure 4.9.

A GUI program has been developed in MATLAB that incorporates the theoretical model developed in this section and allows the user to vary both membrane and back-plate parameters and observe the modified frequency response for the fundamental resonant mode. A depiction of this GUI program is shown on Figure 4.10. The figure shows a design where significant damping has been added with minimal mass loading. While the design satisfies basic geometric requirements, in order to obtain the indicated size and number of holes in the back-plate, a micro-fabrication process is likely required. Such an example is a silicon bulk-micromachining process where a (110)-oriented silicon substrate is masked and anisotropically etched in KOH-water etchant [26]. This process is recommended because it allows for straight-walled holes to be formed, consistent with the desired geometry.

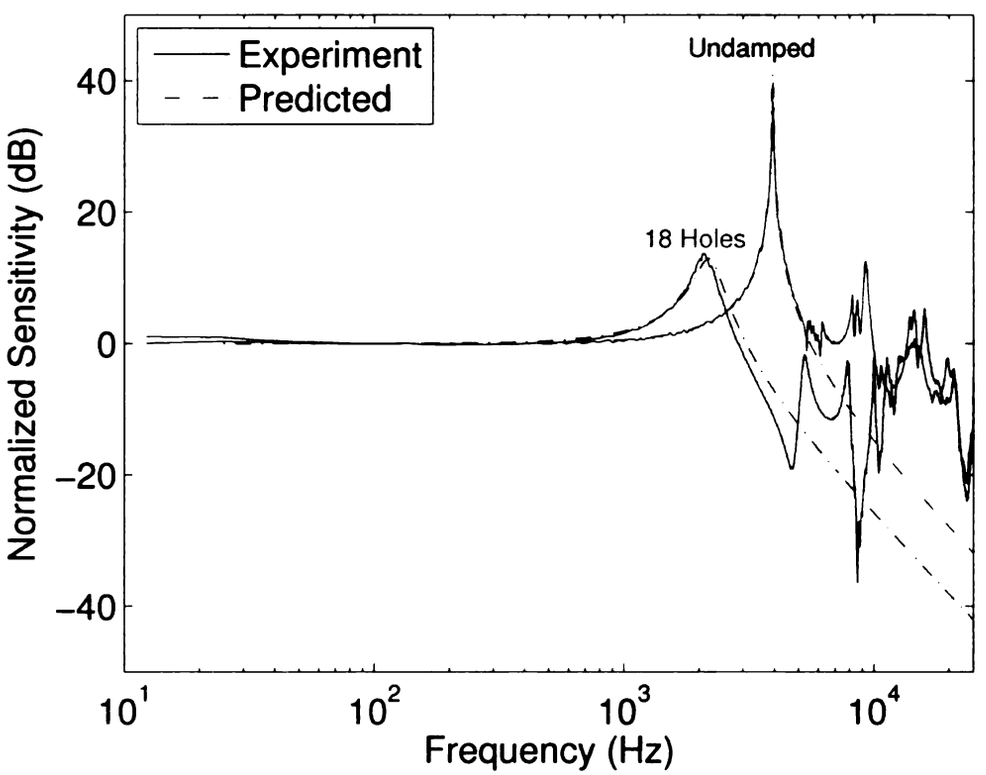

Figure 4.9: Experimental frequency response of microphone membrane with improved perforated insert.

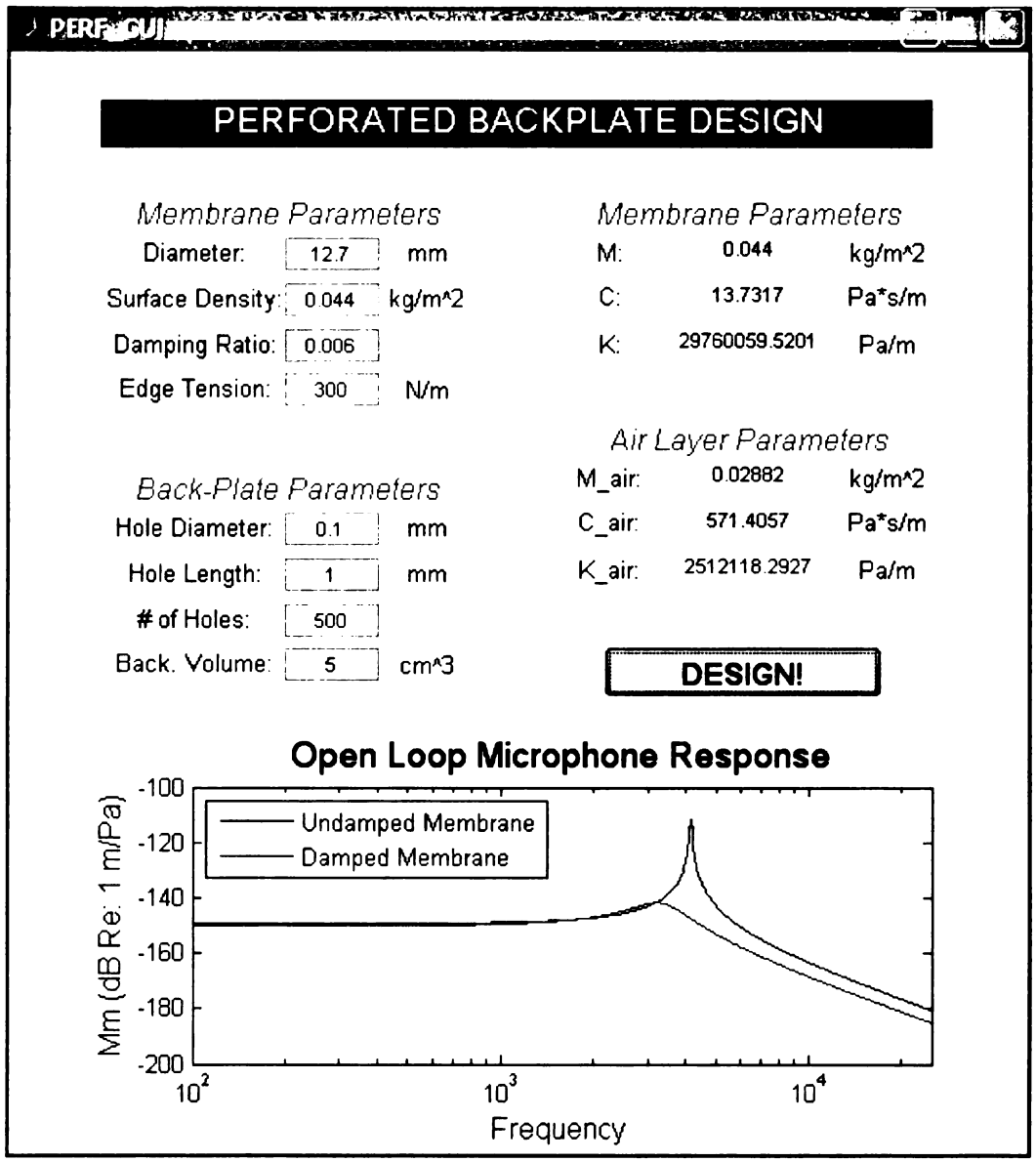

Figure 4.10: Depiction of GUI application used for perforated back-plate design, with "ideal" design of back-plate shown.

Chapter 5

Summary and Conclusions

The present study was undertaken to develop and characterize a novel design of an optical feedback-controlled microphone. The study was motivated by the ultimate use of an array of such microphones in beamforming array measurements used in experimental aeroacoustics.

The 12.7mm prototype presented in Chapter 2 provides a proof of concept of a feedback microphone that is designed using a unique combination of fiber-optic lever sensing and piezoelectric actuation of a PVDF membrane. The results demonstrate that feedback control is effective at modifying sensor dynamics. Furthermore, calibration using electrical actuation of the piezoelectric membrane is demonstrated to be effective in identifying parameters required to theoretically model the membrane's transfer function. The acoustic frequency response of the microphone in open- and closed-loop operation is accurately predicted by the theoretical model, showing a potential for an advanced "self-calibrating"/"self-matching" microphone technology. In such a scheme, severally microphones with initially mismatched parameters in open-loop operation (i.e. stiffness, dampintg) would be calibrated and "matched" such

that they have identical frequency response in closed-loop operation.

Because of the large membrane diameter of the first microphone prototype, the bandwidth of the microphone was limited to 5.1kHz. Therefore, to construct a higher bandwidth sensor a smaller 6.35mm diameter membrane is used in a second prototype. For measurement of the smaller membrane's deflection, an optical sensor with higher sensitivity is needed. For this purpose, a Michelson interferometer is implemented for measurement of the membrane's deflection due to acoustic pressure. The smaller membrane demonstrated the expected higher frequency bandwidth in open-loop operation, while the Michelson interferometer proved to have significantly higher sensitivity than the commercial fiber-optic lever. However, electrical actuation data showed higher order modes that were significantly more prominent than those reported for the 12.7mm prototype. These higher order modes reduced the controllability of the microphone system as they tended to become unstable even with at low feedback gain. Another aspect of the modified sensor design that was investigated was the effect of non-linearity due to the sub-wavelength linear range of the interferometer setup. It is apparent that the sensor can be driven into non-linear operation by an acoustic source, especially at frequencies near its resonance. Specifically, within the microphone's bandwidth, the response became non-linear at and SPL of 110dB. The corresponding SPL near resonance was 90dB dB. This effect could eventually be negated by use of feedback, or by modifications to the membrane prototype and optical sensor.

In Chapter 4, future improvements to the feedback-controlled microphone were discussed employing theoretical arguments in addition to experimental results. In particular, motivated by increasing the feedback control authority of future designs, performance enhancements from the use of an area averaging optical sensor in addition to

a perforated acoustic backplate were described. Both methods are proposed as means for limiting the effect of membrane resonances that are inherent to the vibrational system. First, an area averaging sensor is described. It is demonstrated that the average displacement of higher order resonant modes is significantly lesser in magnitude than the displacement measured at the center of the membrane. It is shown that an optical sensor with a radius that is 0.7 times the membrane radius would provide optimal attenuation of the effect of the first 3 higher order modes. Second, design of a perforated acoustic back-plate was discussed. Acoustic theory was presented to predict the inertial mass, damping, and stiffness contributions that would result from the addition of a back-plate. Experimental results were presented to show the accuracy of the theoretical model when applied to perforated inserts designed for the prototype capsule used in Chapter 2. A GUI application based on this model was created in MATLAB to simplify future designs of perforated back-plates.

The work presented in this thesis shows that, within the limits of stability of the feedback operation, a desired microphone response (e.g. sensitivity, bandwidth, etc.) can be accomplished using the combination of electrical-actuation used for system identification and theoretical modeling used in compensator design. As a result, the feedback microphone concept has several unique advantages: (1) the response of different microphones in a beamforming array can be automatically adjusted to a common desired response, leading to "self-calibrating"/"self-matching" and negating the necessity of an acoustic calibration setup such as a piston-phone, cavity calibrator, or anechoic chamber; (2) the response of the same microphone can be changed to fit different applications by changing the controller parameters; (3) the effects of environmental factors on the microphone's membrane (e.g. temperature, humidity, and dirt) can be minimized or eliminated all together through the feedback. Future work on the feedback-controlled optical microphone concept will include implementa-

tion of the miprovements outlined in Chapter 4 in order to increase the microphone's range of controllabillity. With these improvements in place, in addition to improved sensor packaging and automated controller design, it will become practical to scale up the design to a large sensor count array, where the "self-calibration"/"self-matching" properties are truly valuable.

Chapter 6

Appendix

6.1 Appendix A - Electrical Circuits

6.1.1 Phase-Lead Compensator Circuits

Three different compensator circuits were built and tested in the course of this research. Each used the phase-lead concept, where three independent parameters are adjustable by the user in order to achieve a desired closed-loop response. These parameters are proportional gain (K_p), derivative gain (K_d), and derivative time constant (τ_d). The circuits are op-amp based, and the three independent parameters are controlled by standard potentiometers in circuits #1 and #2, and by digital potentiometers in circuit #3. Descriptions of each circuit's functionality, as well as its construction is given in the following:

Compensator Circuit #1

The first iteration of the phase-lead compensator circuit was designed for ease of setup, albeit with minimal precision. The gain factors, K_p and K_d, are controlled by a combination of rotary switches which set incremental gain values, and potentiometers for variable attenuation. The time constant, τ_d, is varied by a potentiometer. Additionally, DC bias is variable using a potentiometer. A switch on the front panel can be used to control whether the output signal is inverted. Also, switches allow for proportional gain, derivative gain, and DC bias to be individually switched on or off. A schematic diagram of the circuit is shown in Figure 6.1, while a photograph of its front panel is shown in Figure 6.2.

Compensator Circuit #2

The second iteration of the phase compensator circuit was designed to have higher precision in selecting phase-lead parameter values, while sacrificing some of the ease of setup of the first version. A breadboard was used for construction of the compensator prototype, as shown in Figure 6.3. The schematic diagram of this circuit is depicted in Figure 2.4. In this version of the circuit, each of the resistor and capacitor values have been been measured and are listed in Table 6.1. The phase lead parameters, K_p, K_d, and τ_d are set by the trim-pots R_p, R_d, and R_c, respectively. The desired values for these trim-pots are determined using design software (see later section), and are measured using a multimeter before being placed in the circuit.

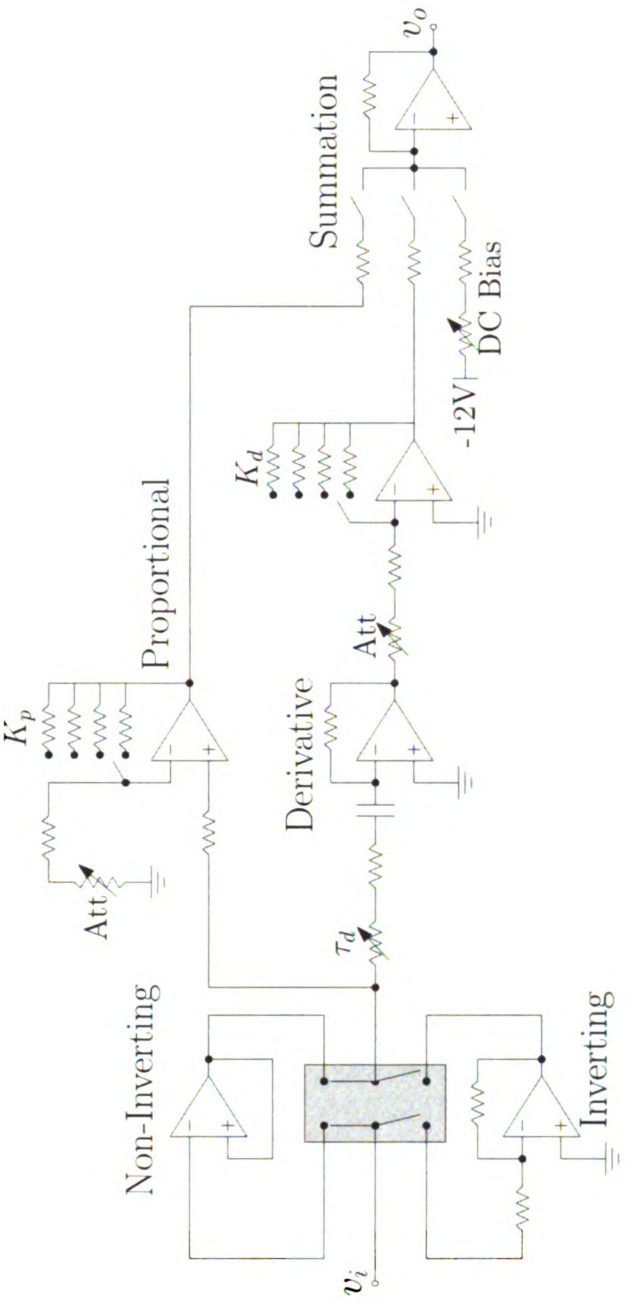

Figure 6.1: Schematic diagram of first phase-lead compensator circuit.

Compensator Circuit #3

A third compensator circuit was designed and built that incorporates digital potentiometers for setting the three phase-lead compensator parameters. In this way, the

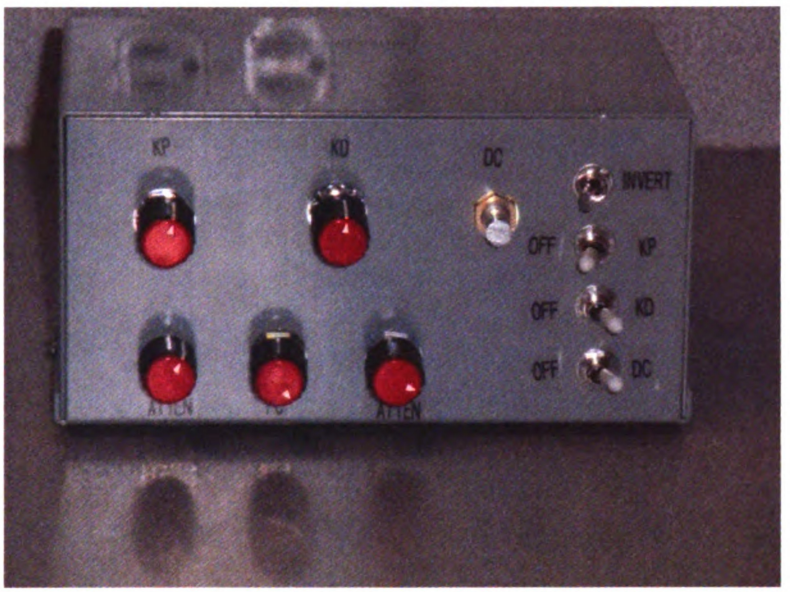

Figure 6.2: Photograph of front panel of first phase-lead compensator circuit.

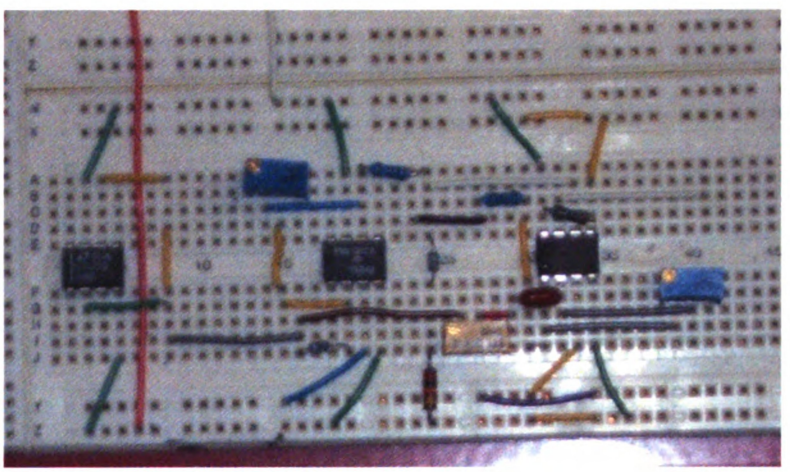

Figure 6.3: Photograph of second phase-lead compensator on a breadboard.

compensator circuit is automated in such a way that is desirable for large sensor count arrays where it is impractical for the user to individually set the values of standard potentiometers. A photograph of this circuit is shown in Figure 6.4.

The digital potentiometers used are of the MCP42XXX variety by Microchip Technologies[1]. These chips have two on-board potentiometers each with 256 incremental

[1] `http://ww1.microchip.com/downloads/en/DeviceDoc/11195c.pdf`

Table 6.1: Electrical components used in phase-lead controller circuit depicted in Figure 2.4

Symbol	Type	Value
$OA1$	Op-amp	L1220
$OA2$	Op-amp	OP27
$OA3$	Op-amp	AD827
$OA4$	Op-amp	AD827
R_{p1}	Resistor	1.49 kΩ
R_{p2}	Resistor	0.996 kΩ
R_{d2}	Resistor	0.998 kΩ
$R_{f,sum}$	Resistor	9.98 kΩ
R_{DC}	Resistor	23.72 kΩ
R_p	Trim-pot	Variable
R_c	Trim-pot	Variable
R_d	Trim-pot	Variable
C	Capacitor	0.082 μF

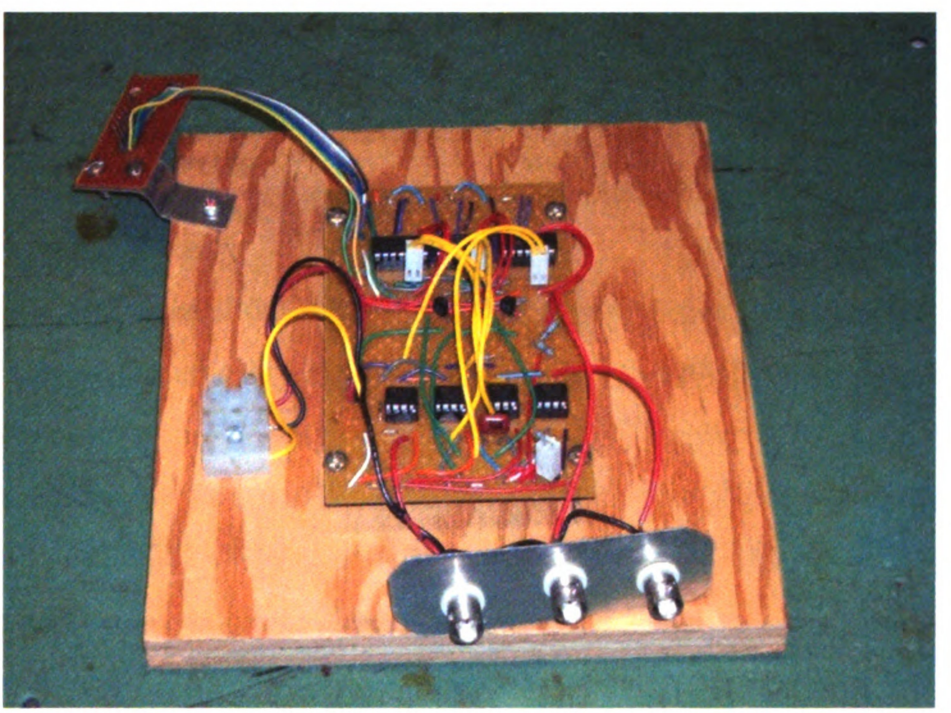

Figure 6.4: Photograph of third phase-lead compensator circuit.

resistance settings. The resistance can be programmed using a three wire serial interface. The three pins used for programming are SI, SCK, and $\overline{\text{CS}}$. The SI (signal in)

pin is where the 16 bit input is recorded. The first 8 bits, or command byte, of this signal determine which on-board potentiometer will be programmed, where the 8 bit number 17 (00010001) selects potentiometer 0, 18 (00010010) selects potentiometer 1, and 19 (00010011) selects both potentiometers. The command byte is followed by the data byte which selects a resistance increment from 0-256. The signal is clocked in by the SCK (signal clock) pin, where each bit is recorded on the rising edge of the digital clock waveform. The $\overline{CS}$ (chip select) pin should be asserted low immediately before programming the chip. When the $\overline{CS}$ pin is asserted high at the end of the programming cycle, the chip will be set to its newly assigned resistance value. An example digital waveform for programming of a MCP42XXX variety chip is shown in Figure 6.5. In this example, the user is selecting potentiometer 0 to be programmed to its 50th resistance increment (corresponding to approximately 2kΩ for a MCP42010 chip). Thus, the full 16 bit signal input at the SI pin is 00010001 00110010. For purposes of the current application the $\overline{SHDN}$ (shutdown) and $\overline{RS}$ (reset) pins should always be asserted high, and are thus connected to the +5V power supply.

An interesting feature of the MCP42XXX series of digital potentiometers is the presence of the SO (signal out) pin. Using this pin, multiple chips can be daisy chained in such a manner that a large number of chips can be programmed from a single three wire interface. This is achieved by wiring the SO pin of one chip to the SI pin of the next, where the SCK and $\overline{CS}$ connections are shared. In this configuration, when the first chip receives a signal longer than the standard 16 bits, it will pass this first signal to the chip connected to its SO pin, and record instead the next 16 bits it receives. Using this method, it is assumed that compensator circuits for thirty or more microphones can be controlled using a single computer interface.

In the current circuit, MCP42050 (50kΩ), MCP42100 (100kΩ), and MCP42010 (10kΩ)

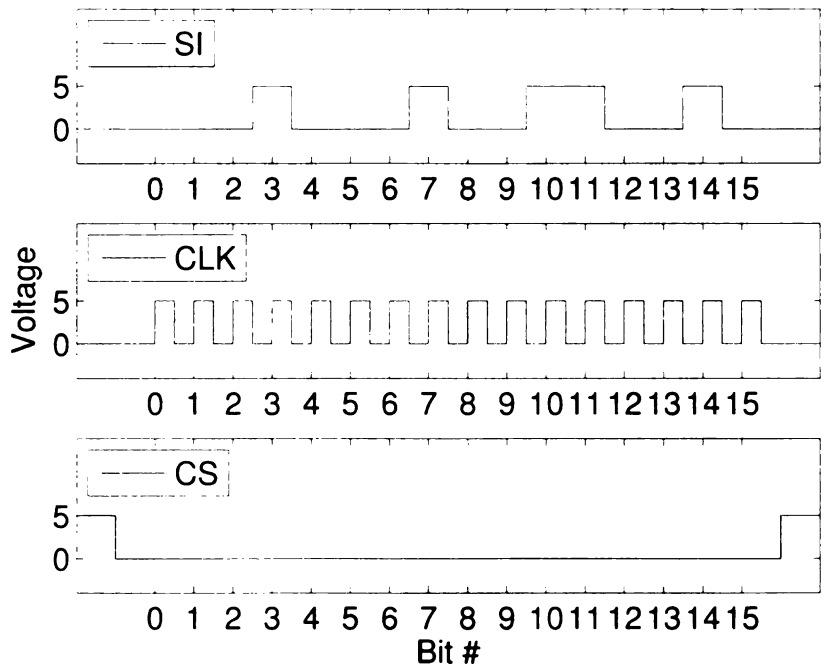

Figure 6.5: Example digital waveform used in programming a MCP42XXX series digital potentiometer. The example case is for programming potentiometer 0 to position 50, where the full 16 bit input is 00010001 00110010.

chips were chosen to control K_p, K_d, and τ_d respectively. These values were chosen for the design because they provided a range of gain values that were typical in designs for the first microphone prototype. Future designs may use different components, depending if more/less gain is desired. In the circuit, the two on-board potentiometers of each chip are wired in parallel. In this configuration, assuming both potentiometers to be identical, each chip will provide over 30,000 unique resistance increments. A table listing components used in the compensator circuit is given in Table 6.2.

Calculation of resistance values and determination of required potentiometer settings is performed by a LabView application, to be described later. The circuit includes two enhancement mode MOSFETs which are used for switching of the circuit. The source and drain pins of these MOSFETS are connected to the input pins of the

Table 6.2: Electrical components used in serial interfaced phase-lead controller depicted in Figure 3.7

Symbol	Type	Value
$OA1$	Op-amp	LM741
$OA2$	Op-amp	LM741
$OA3$	Op-amp	LM741
$OA4$	Op-amp	LM741
R_{p1}	Resistor	1.496 kΩ
R_{p2}	Resistor	1.808 kΩ
R_{d2}	Resistor	1.798 kΩ
$R_{f,sum}$	Resistor	19.92 kΩ
R_{test}	Resistor	19.92 kΩ
R_{DC}	Resistor	46.8 kΩ
R_p	Digital Pot	MCP42050
R_c	Digital Pot	MCP42010
R_d	Digital Pot	MCP42100
C	Capacitor	0.022 μF
M_1	MOSFET	NTE490
M_2	MOSFET	NTE490

op-amps for the proportional and derivative gain sections. When a high voltage is asserted at the gate of either of these MOSFETS, current will be allowed to flow from the source to the drain, effectively shorting the input pins of the op-amp and turning it "off". Alternately, when a low voltage is asserted no current will be allowed to flow, thus turning that op-amp "on". In total, including power supply, seven wires are used.

6.1.2 Michelson Interferometer Control Circuit

During construction of the Michelson interferometer it was observed that there was a low frequency (sub 1Hz) drift in the sensor's output, resulting in the sensor drifting out of its desired set-point. In order to maintain the output of the sensor at this setpoint, feedback was employed using a mirror mounted on a piezoelectric stack.

The schematic shown in Figure 3.6 was designed for the purpose of low frequency fringe-locking of the interferometer signal. A photograph of this circuit is shown in Figure 6.6, and a list of components is given in Table 6.3.

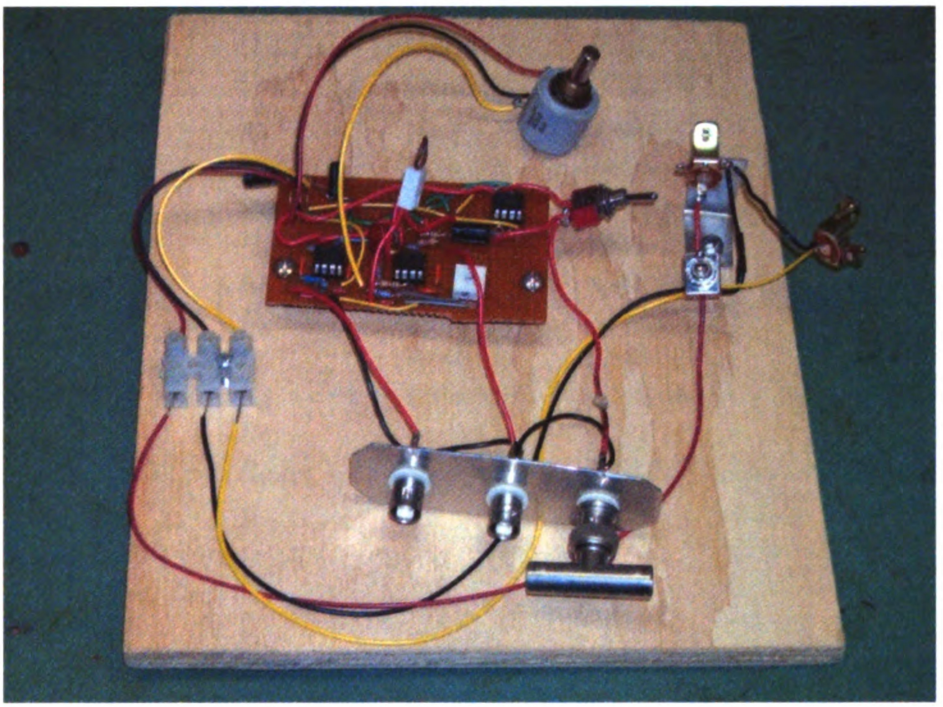

Figure 6.6: Photograph of Michelson interferometer control circuit.

6.1.3 Other Circuits

Signal Amplifier and Variable Low Pass Filter

A signal amplifier was constructed with variable gain and low pass filter options. The circuit is single input/single output. It can be powered either by a 9V battery or by a DC adapter plug. The gain level is controlled by a rotary switch, where the selectable gain values are 1.01, 3.15, 10.2, 39.7, and 100, as determined by experimental calibration. The corner frequencies of the low pass filter are also controlled by a rotary switches, and are 340Hz, 620Hz, 3200Hz, 11,700Hz, and 32,000Hz. A capacitor is

Table 6.3: Electrical components used in Michelson interferometer control circuit depicted in Figure 3.6

Symbol	Type	Value
$OA1$	Op-amp	TLO72
$OA2$	Op-amp	TLO72
$OA3$	Op-amp	TLO72
$OA4$	Op-amp	TLO72
R_1	Resistor	0.996 kΩ
R_2	Resistor	2.000 kΩ
R_3	Resistor	2.004 kΩ
R_4	Resistor	19.92 kΩ
R_5	Resistor	100 kΩ
R_6	Resistor	0.984 kΩ
R_7	Resistor	1.804 kΩ
R_8	Resistor	1.798 kΩ
R_9	Resistor	0.984 kΩ
R_{DC}	Resistor	4.64 kΩ
R_G	Trim-pot	Variable
P_{set}	Potentiometer	1 kΩ
C_1	Capacitor	1 μF
C_2	Capacitor	100 μF

placed at the input of the circuit such that the output is AC coupled with a corner frequency of 1.6Hz. A schematic of the signal amplifier and variable low pass filter is shown in Figure 6.7, and photograph of the circuit is shown in Figure 6.8.

Third Order Inverse Chebyshev Filter

A filter circuit was constructed for the purpose of sharply cutting off the effect of resonant modes in the microphone's response. The type of filter that was constructed for this purpose is the Third order inverse Chebyshev filter. The frequency response of such a filter can be described as having a single sharp notch with a 20dB/decade roll-off above the notch frequency. The filter is designed using a Texas instruments

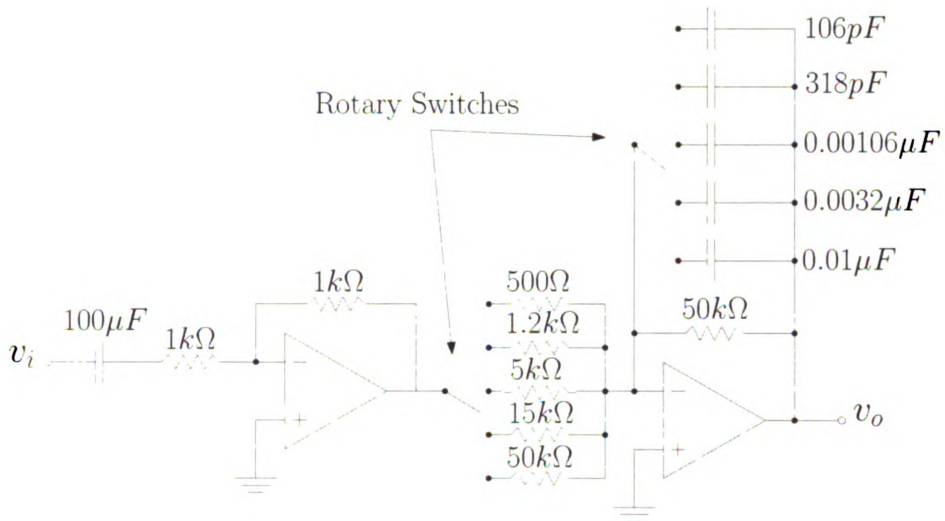

Figure 6.7: Schematic diagram of signal amplifier and variable low pass filter circuit.

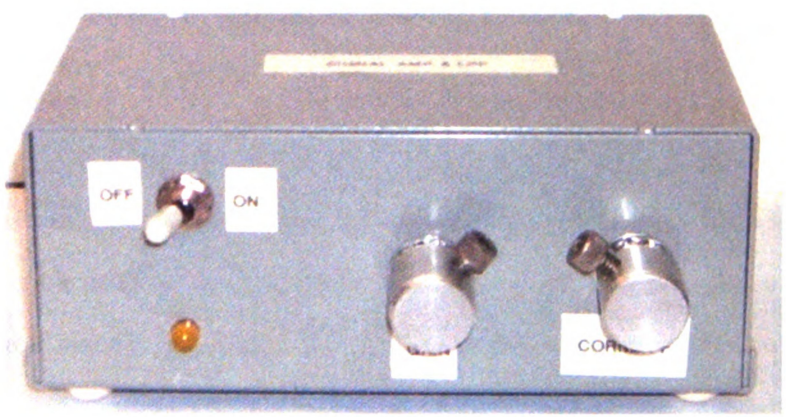

Figure 6.8: Photograph of signal amplifier and variable low pass filter circuit.

UAF42 Universal Active Filter chip[2]. The design program FILTER42[3] can be used to determine the values for the three external resistances that control notch frequency, R_P, R_{F1}, and R_{F2}. Using the same filter chips, a variety of other filter types such as Butterworth, Bessel, and Chebyshev can be constructed. A photograph of the Inverse Chebyshev filter circuit is shown in Figure 6.9.

[2]UAF42 datasheet - `http://focus.ti.com/lit/ds/symlink/uaf42.pdf`
[3]FILTER42 manual - `http://focus.ti.com/lit/an/sbfa002/sbfa002.pdf`

Figure 6.9: Photograph of inverse Chebyshev filter circuit.

Power Amplifier

A LM386 chip was used to construct a small power amplifier circuit. The output of this circuit can be used to amplify an audio signal to a speaker, with a peak output power of approximately one watt. The circuit is single input/single output and has a potentiometer providing variable gain. A photograph of the 386 power amplifier circuit is shown in Figure 6.10.

6.2 Appendix B - Software Applications

6.2.1 FeedbackGUI

For simplification of the feedback-controlled optical microphone's operation, and for future scalability for large arrays, a single application has been designed to handle

Figure 6.10: Photograph of 386 power amplifier circuit.

all computational and serial interfacing needs. The program has been written using the LabVIEW programming environment. The functions of the LabVIEW application include (1) calibration of the microphone's frequency response, (2) identification of the open-loop transfer function, (3) calculation of the closed-loop transfer function and compensator settings based on the user's desired response, and (4) programming of the compensator through the digital input/output interface of the National Instruments PCI-6024E DAQ board. Two versions of the program exist. In the first variation, FeedbackGUI_V1.vi, the user specifies closed-loop DC attenuation, natural frequency and β, and calculations are performed to determine the required K_p, K_d, and τ_d. In the second variation, FeedbackGUI_V2.vi, the user specifies K_p, K_d, and τ_d, and calculations are performed to determine DC attenuation, natural frequency, and β. Each of the functions of the GUI will be described in detail below.

Calibration stage

The first portion of the Feedback GUI application is the calibration section. This is used to calibrate the microphone's frequency response in an electrical actuation

test using a harmonic sweep waveform. The user inputs a sampling frequency, number of records, and number of samples per record. When the program runs, the signal waveform is plotted along with spectra of the signal for the current record. An autospectra is performed to get the power spectra of both the reference signal and the microphone actuation signal. Cross spectrum analysis is used to determine the sensitivity and phase of the electrical actuation signal relative to the reference signal.

To maximize the signal to noise of the electrical actuation calibration, for each record only the seven frequency bins near the peak of the reference signal are kept. This methodology is practical only when using a long duration harmonic sweep waveform, as this signal will only pass through a small fraction of the calibration frequency range for any single record. After completion of the calibration cycle, sensitivity and phase for like frequency bins are averaged, and plotted in the front panel. The user also has the option of saving this calibration data in a .txt file, where the data is saved in columns containing frequency, sensitivity, phase, reference spectra, and electrical actuation spectra.

System Identification Stage

Using the sensitivity and phase results obtained using electrical actuation, system identification is performed to determine open-loop parameters of the microphone. The system identification is performed using the methodology discussed in Chapter 2. The user specifies a film thickness, which is used to calculate mass. Calculations for damping ratio, stiffness, and electrical actuation sensitivity are performed using a MathScript node.

Closed-Loop Specification Stage

There are two Feedback GUI applications that have been developed, with the difference between the two being the methodology used for calculations. In the first version, FeedbackGUI_V1.vi, the user specifies closed-loop DC attenuation, natural frequency, and angle β, and the subVI GcSpec_V1.vi computes the required phase-lead parameters K_p, K_d, and τ_d needed to achieve this closed-loop response. In the second version, FeedbackGUI_V2.vi, K_p, K_d, and τ_d are directly specified by the user and DC attenuation, natural frequency, and β are computed in the subVI GcSpec_V2.vi. In both cases, the theoretical frequency response for both open- and closed-loop are plotted.

Controller Programming Stage

After the phase-lead parameters have been determined, the compensator is programmed using a serial interface. First, the necessary settings for the digital potentiometers are determined. Ideal resistance is determined based on the known component values in the compensator circuit. The program then does a table lookup to determine the digital potentiometer setting with minimum error from this ideal resistance. The potentiometer settings and corresponding resistance values are contained in the files Rp_Vsort.txt, Rd_Vsort.txt, and Rc_Vsort.txt. Once these settings have been determined, they are passed to the subVI ProgramChips.vi. This program creates the digital signal waveforms (see Figure 6.5) for the SI, SCK, and $\overline{\text{CS}}$ wires, and passes them through the digital output of the National Instruments board. Additionally, the controller can be switched on and off, and re-programmed multiple times from a single calibration.

6.2.2 MATLAB Software

PhaseLeadGUI

PhaseLeadGUI is a MATLAB GUI application that loads an electrical actuation calibration file and uses this to calculate the phase lead compensator transfer function required to satisfy some user specified closed-loop response. To use this program, open and run the PLC_GUI.m file, and enter the name of the electrical actuation calibration file that will be used in the field provided. The program allows the user to then input their desired closed-loop parameters. After pressing the DESIGN! button, the program will run computations based on the analytical method described in Chapter 2. The results of these computations are displayed on the right side, and theoretical closed-loop response is plotted (note: the component values output by the program are those that would be required for the circuit used in the second phase-lead compensator design. For different circuits, refer to the phase lead parameters on the upper right and adjust component values as necessary).

It should be mentioned that at times the program will output a negative value for one or more of the phase-lead parameters. This indicates that particular set of closed-loop parameters cannot be achieved using the basic method outlined in Chapter 2. The user should adjust the specified closed-loop response until the program outputs a realistically achievable set of phase-lead parameters.

DigitalPot.m

DigitalPot is a MATLAB GUI application used to determine the necessary settings of the digital potentiometers used in the third phase-lead compensator circuit. The

user inputs values for K_p, K_d, and τ_d. The program then calculates required resistance values based on the components used in the compensator circuit given in Table 6.2. Then, based on calibration of the digital potentiometers' incremental resistance, settings are determined that will minimize the error between the desired resistance and the actual resistance of the digital potentiometer. The frequency response of the desired compensator is then plotted with the theoretical response of the actual compensator.

Perforated Backplate GUI

The perforated backplate GUI application is designed to simulate the open-loop response of a microphone where a perforated back-plate has been added to increase damping. Simulations are based on the analysis described in Chapter 4. To use this program, open and run the PERF_GUI.m file. The user will then specify values for the unmodified membrane parameters, which by default are set to values similar to those of the prototype microphone from Chapter 2. Then the user may specify geometric parameters for the back-plate. After pressing the DESIGN! button, the program will compute the air layer properties and plot the theoretical response of the un-modified membrane in addition to the response of the membrane with the addition of a perforated back-plate.

PLC_Solver.m

PLC_Solver.m is a MATLAB function file used to calculate phase-lead parameters based on a set of inputs. The first required input is the OL_Parameters vector which includes mass, damping, stiffness, and electrical actuation sensitivity taken from cali-

bration data or manually inputted. The other inputs are the user desired closed-loop DC attenuation, natural frequency, and angle β. The program runs computations based on the analysis described in Chapter 2. The program outputs the phase lead parameters K_p, K_d, and τ_d, as well as resistor values required for the second compensator circuit.

EstimateMembrane.m

EstimateMembrane.m is a MATLAB function file used to estimate the membrane's mass, damping, stiffness, and electrical actuation sensitivity from electrical actuation calibration data. The program requires a matrix taken from a calibration file as well as a membrane thickness input. The calibration data should be formatted in such a way that its first column is a frequency vector and the second column is sensitivity measured as the output of the lever sensor relative to the signal from the function generator.

BIBLIOGRAPHY

[1] Humphreys, W.M., T.F. Brooks, W.W. Hunter, and K.R. Meadows, *Design and Use of Microphone Directional Arrays for Aeroacoustic Measurements*, 36st Aerospace Sciences Meeting & Exhibit, AIAA Paper number 98-0471, Reno, NV, Jan 12-15 (1998)

[2] Brooks, T.F., W.M. Humphreys, *A deconvolution approach for the mapping of acoustic sources (DAMAS) determined from phased microphone arrays*, Journal of Sound and Vibration **294**, 856-879 (2006)

[3] Zuckerwar, A.J., *Measurements, Acoustical*, Encyclopedia of Applied Physics **9**, 491-514 (1994)

[4] Arnold, D.P., T. Nishida, L.N. Cattafesta, M. Sheplak, *A directional acoustic array using silicon micromachined piezoresistive microphones*, J. Acoust. Soc. Am. **113** 1, 289-298 (2003)

[5] Horowitz, S., T. Nishida, L.N. Cattafesta, M. Sheplak, *Development of a micromachined piezoelectric microphone for aeroacoustics applications*, J. Acoust. Soc. Am. **122** 6, 3428-3436 (2007)

[6] Martin, D., J. Liu, K. Kadirvel, R. Fox, M. Sheplak, T. Nishida, *A Micromachined Dual-Backplate Capacitive Microphone for Aeroacoustic Measurements*, J. Microelectromechanical Systems, **16** (6), 1289-1302 (2007)

[7] Martin, D., K. Kadirvel, T. Nishida, M. Sheplak, *An Instrumentation Grade MEMS Condenser Microphone for Aeroacoustic Measurements*, 46th Aerospace Sciences Meeting & Exhibit, AIAA Paper number 2008-257, Reno, NV, Jan 7-10 (2008)

[8] Ko, S., Y. Kim, S. Lee, S. Choi, S. Kim, *Micromachined piezoelectric membrane acoustic device*, Sens. Actuators. A, **103**, 130-134 (2003)

[9] Lee, W., N.A. Hall, Z. Zhou, F.L. Degertekin, *Fabrication and characterization of a micromachined acoustic sensor with integrated optical readout*, IEEE J. Sel. Top. Quantum Electron. **10** (3), 643-651 (2004)

[10] Hall, N.A., B. Bicen, M.K. Jeelani, W. Lee, *Micromachined microphones with diffraction-based optical displacement detection*, J. Acoust. Soc. Am. **118** (5), 3000-3009 (2005)

[11] Bechhoefer, J., *Feedback for physicists: A tutorial essay on control*, Reviews of Modern Physics, **77**, 788-789 (2005)

[12] Keating, D.A., *Force Feedback Microphone*, Proc. Inst. Acoust. **8** (6), 67-73 (1986)

[13] Karatzas, L.S., D.A. Keating, M.J. Usher, *A practical optical force-feedback microphone*, Transactions of the Institute of Measurement and Control. **16** (2), 75-85 (1994)

[14] Edelson, J.S., N.P. Ward, *Force Balance Microphone*, U.S. Patent No. 6,285,769, Sep. 4, 2001

[15] Bicen, B.B., S. Jolly, K. Jeelani, C.T. Garcia, N.A. Hall, F.L. Degertekin, Q. Su, W. Cui, R.N. Miles, *Integrated Optical Displacement Detection and Electrostatic Actuation for Directional Optical Microphones with Micromachined Biomimetic Diaphragms*, IEEE Sensors Journal, **9** (12), 1933-1941 (2009)

[16] Tamura, M., T. Yamaguchi, T. Oyaba, T. Yoshimi, *Electroacoustic Transducers with Piezoelectric High Polymer Films*, 49th Convention of the Audio Engineering Society, New York, NY, Sept. 10 (1974)

[17] Lerch, R., *Electroacoustic transducers using piezoelectric polyvinylideneflouride films*, J. Acoust. Soc. Am. **66** 4, 952-954 (1979)

[18] Howarth, T.R., J.F. Tressler, J.A. Bucaro, *Piezoelectric Acoustic Actuator*, U.S. Patent No. 6,717,337, Apr. 6, (2004)

[19] Doebelin, E.O., *Measurement Systems, Application and Design* - 4th ed. McGraw-Hill, New York (1990)

[20] Hu, A., F. Cuomo, A. Zuckerwar, *Theoretical and experimental study of a fiber optic microphone*, J. Acoust. Soc. Am. **91** (5), 3049-3056 (1992)

[21] Zuckerwar, A.J., F. Cuomo, T. Nguyen, S. Rizzi, and S. Clevenson, *High-temperature fiber-optic lever microphone*, J. Acoust. Soc. Am. **97** (6), 3605-3616 (1995)

[22] Meirovitch, L. *Analytical Methods in Vibrations*, MacMillan, New York (1967)

[23] Kinsler, L., A.R. Frey, A.B. Coppens, J.V. Sanders, *Fundamentals of Acoustics* –3rd ed. John Wiley & Son, New York (1982)

[24] Philips, C.L., R.D. Harbor, *Feedback Control Systems* –4th ed. Prentice Hall, New Jersey (2000)

[25] Zuckerwar, A.J., *Principles of Operation of Condenser Microphones*, AIP handbook of condenser microphones, theory calibration and measurements, 45-57, AIP Press, New York (1994)

[26] Mehregany, M., W.H. Ko, A.S. Dewa, C.C. Liu, *Microfabrication and Micromachining*, Microelectromechanical Systems and the Multiuser MEMS Processes, Part I: MEMS Overview. 22-39, Case Western Reserve University – MCNC Short Course Handbook. Case Western Reserve University, Cleveland OH. December 4-6, 1995.